EXPERIMENTS AND ANALYSIS OF AQUEOUS ELECTRODE PROCESSING FOR ENERGY STORAGE

A Thesis

by

DEEPAK BHATIA

Submitted to the Office of Graduate and Professional Studies of
Texas A&M University
in partial fulfillment of the requirements for the degree of

MASTER OF SCIENCE

Chair of Committee,	Partha P. Mukherjee
Committee Members,	Debjyoti Banerjee
	Sarbajit Banerjee
Head of Department,	Andreas A. Polycarpou

May 2016

Major Subject: Mechanical Engineering

ABSTRACT

There is an ever-growing demand for Lithium-Ion Batteries in a widespread series of applications, where battery life and reliability are of key importance. There exist novel materials that are helping increase battery reliability and life but there is a lack of environment friendly and cost-effective processing techniques that are used to produce such energy storage devices. Current processing techniques use N-methyl-2-pyrrolidone as a solvent for electrode slurry, which is expensive and has the potential to damage the environment, increasing the risk of cancer and reproductive toxicity. Therefore, there is a need to move towards a solvent that is environmentally friendly, cheap to produce and can serve as a potential replacement. In this work, the use of deionized water has been experimentally evaluated to create an electrode processing technique that could become an environmentally friendly and cost-effective technique to produce Lithium-Ion Batteries.

This study focuses on the concepts of Lithium-Ion Batteries and their current electrode processing techniques. The proposed Aqueous Processing technique for electrode manufacture is discussed in detail along with a discussion of challenges currently being faced in this area. A 1-D physics based drying model is also developed as part of this study that is based upon evaporation, diffusion and sedimentation.

My analysis has shown that the proposed Aqueous Processing can be implemented using low-cost preparation methods and deionized water. Drying temperature has an effect on the agglomeration of particles that could impact the electrochemical

performance of the electrode. My analysis has also shown that an optimal amount of dispersant needs to be added to reduce the effect of agglomeration while maintaining good film adhesion. The results from the 1-D show that at a higher drying temperature a larger volume fraction is observed at the top surface of the electrode.

ACKNOWLEDGEMENTS

I would like to thank my committee chair, Dr. Partha P. Mukherjee, for his support and guidance during my time in ETSL as a Master of Science student. He has always inspired me to perform high impact research and follow my dreams. I would also like to thank my committee members, Dr. Debjyoti Banerjee, and Dr. Sarbajit Banerjee, for their guidance and support throughout the course of this research.

Thanks goes to the department faculty and staff for their assistance over the last two years. I also want to thank my colleagues in ETSL that have made my graduate experience memorable and for their support during the Master of Science program.

Finally, thanks to my family, Carmen and her family for the support and encouragement in completing my thesis and graduate studies.

NOMENCLATURE

D	Diffusion constant (m^2/s)
E	Rate of evaporation of water (m/s)
U	Sedimentation velocity (m/s)
H_0	Initial film height (m)
k	Boltzmann constant (J/K)
R	Particle/aggregate radius (m)
Pe	Peclet number (-)
Pe_{sed}	Peclet sedimentation number (-)
N_s	Sedimentation number (-)
T	Temperature (K)
t	Time (s)
$\bar{t}$	Dimensionless time (-)
y	Vertical position in film (m)
$\bar{y}$	Dimensionless film position (-)
ϕ	Volume fraction (-)
ϕ_m	Upper limit on volume fraction (-)

TABLE OF CONTENTS

Page

ABSTRACT ii

ACKNOWLEDGEMENTS iv

NOMENCLATURE v

TABLE OF CONTENTS vi

LIST OF FIGURES vii

LIST OF TABLES xi

CHAPTER I INTRODUCTION AND LITERATURE REVIEW 1

CHAPTER II AQUEOUS PROCESSING IN LIBS 11

- Experimental Equipment 11
- Materials 18
- Cathode and Coin Cell Preparation 19
- Results and Discussion 27

CHAPTER III PHYSICS OF ELECTRODE DRYING 58

- Model 59
- Results and Discussion 66

CHAPTER IV SUMMARY AND FUTURE RECOMMENDATIONS 75

REFERENCES 77

LIST OF FIGURES

Page

Figure 1: Cost breakdown for LIB production [28] 4

Figure 2: Challenges in Aqueous Processing 9

Figure 3: Schematic of a Lithium-Ion Battery 11

Figure 4: Schematic overview of the steps utilized for Aqueous Processing 12

Figure 5: Aluminum foil and paper cutter 13

Figure 6: OHAUS Analytical Scale 13

Figure 7: Powdered materials with mortar and pestle 14

Figure 8: IKA tube mixing platform 15

Figure 9: Magnetic mixing platform 15

Figure 10: Elcometer for casting films 16

Figure 11: MTI oven 16

Figure 12: Hole punch 16

Figure 13: Glovebox 17

Figure 14: Crimper in the glovebox 17

Figure 15: Arbin BT2000 18

Figure 16: MTI BST8-MA 18

Figure 17: PEI, XG and DI water solution (top view) 22

Figure 18: Final electrode slurry 22

Figure 19: Casted cathode sheet 23

Figure 20: Dried cathode sheet 23

Figure 21: Electrode sheet shown with punched cathode 24

Figure 22: Coin cell components displayed in order of placement within cell [58] 25

Figure 23: Representative baseline performance of in-house Organic Processing 28

Figure 24: Performance of cells fabricated using Organic Processing 30

Figure 25: Charge and discharge curves for a representative cell prepared using Organic Processing 31

Figure 26: Performance comparison of 80:10:10 wt % and 70:20:10 wt % (Organic Processing).....33

Figure 27: Baseline comparison between Aqueous and Organic Processing 34

Figure 28: Performance of cells created using Aqueous Processing 35

Figure 29: Charge and discharge curve for a representative cell prepared using Aqueous Processing.....36

Figure 30: Performance comparison between cells prepared using Organic and Aqueous Processing.....36

Figure 31: Cathode electrode sheets dried at different temperature (Aqueous Processing).....38

Figure 32: Performance comparison of cells prepared from electrode sheets dried at different temperatures (Aqueous Processing).....39

Figure 33: Charge and discharge curves for a cell from each electrode sheet cycled at C/5.....40

Figure 34: Charge and discharge curves for a cell from each electrode sheet cycled at C/2.....40

Figure 35: Charge and discharge curves for a cell from each electrode sheet cycled at 1C.....40

Figure 36: Average performance comparison of cells from different temperature dried electrode sheets under several operating conditions.....44

Figure 37: Performance of 3 cells prepared from an aqueous sheet dried at 50˚C 44

Figure 38: Aqueous Processing at 50˚C.....45

Figure 39: Organic Processing at 50˚C 46

Figure 40: SEM image of a cathode dried at 70˚C.....47

Figure 41: SEM image of a cathode from 30˚C 47

Figure 42: SEM image of a cathode from approximately 21˚C 48

Figure 43: PEI creates a layer of positive charge around LFP to prevent agglomeration 50

Figure 44: Aqueous sheet dried at 50˚C with 6% XG and 4% PEI by mass 51

Figure 45: Aqueous sheet dried at 50˚C with 7% XG and 3% PEI by mass 52

Figure 46: Aqueous sheet dried at 50˚C with 8% XG and 2% PEI by mass 52

Figure 47: Aqueous sheet dried at 50˚C with 9% XG and 1% PEI by mass 52

Figure 48: Performance comparison between cells with various binder and dispersant concentrations 53

Figure 49: Performance comparison between no PEI (10:0 wt %) and 3-wt % PEI (7:3) 54

Figure 50: Performance comparison between no PEI (10:0 wt %) and 2-wt % PEI (8:2 wt %) 55

Figure 51: SEM image with 9% XG and 1% PEI by mass 56

Figure 52: SEM image with 8% XG and 2% PEI by mass 56

Figure 53: SEM image with 7% XG and 3% PEI by mass 57

Figure 54: SEM image with 6% XG and 4% PEI by mass 57

Figure 55: Progression of slurry drying and film formation 58

Figure 56: Validation of present model with Ns = 1, Pe = 10 67

Figure 57: Validation of present model with Ns = 1, Pe = 1 67

Figure 58: Evaporation rate as a function of temperature (˚C) and relative humidity (-) 69

Figure 59: Comparison between Peclet and Sedimentation numbers at different drying temperature 70

Figure 60: Volume fraction evolution with Aqueous Processing at 70˚C 71

Figure 61: Volume fraction evolution with Aqueous Processing at 50˚C 71

Figure 62: Volume fraction evolution with Organic Processing at 50˚C.....72

Figure 63: Volume fraction evolution at the top surface at different drying temperature with Organic and Aqueous Processing.....73

LIST OF TABLES

Page

Table 1: Comparison between different battery chemistries [13] 2

Table 2: Comparison between Organic and Aqueous Processing for LIB electrodes 6

Table 3: Non-dimensional inputs for water at different temperatures 68

CHAPTER I

INTRODUCTION AND LITERATURE REVIEW

Lithium-Ion Batteries (LIBs) are amongst the most popular sources for energy storage in a wide range of applications ranging from consumer electronics to vehicle electrification in Electric and Hybrid Electric Vehicles (EVs and HEVs, respectively). Over the years there has been an increase in the consumer base for portable electronics and EVs, which has lead to an increase in production and dependence on highly efficient LIBs [1-3]. The increase in energy demands is not restricted to portable electronics and EVs, as LIBs are now being considered to be a possible energy storage system for energy grids to improve grid reliability [4-6]. There is tremendous research effort into the creation of new, stable, high-powered LIB electrochemistry to improve overall capacity and life [7, 8]. A great number of studies have investigated the effects of electrode thickness, porosity of the microstructure and general composition but have not focused on the environmental impact that is associated in creating high-performance batteries [9-12].

Lithium-Ion Batteries have gained popularity over the years and are now commanding a much greater market share due to their high energy density as compared to their Lead-acid or Nickel Metal Hydride competitors. These batteries have a longer cycle life and low degradation over their lifetime when not in operation [13-15]. LIBs are commanding the energy storage market since they are a significant improvement in terms of specific energy, energy density and coulometric efficiency as shown in Table 1.

	Lead-acid	Nickel-Metal Hydride	Lithium-Ion
Specific energy (Wh/kg)	35	75	150
Energy density (Wh/L)	70	240	400
Coulometric efficiency	0.8	0.65-0.70	>0.85

Table 1: Comparison between different battery chemistries [13]

Even though many studies have focused on creating high-reliability batteries, there have been very few efforts in to the creation of processing techniques for LIBs that are environmentally friendly and cost- effective [1, 16, 17]. Therefore, extensive efforts are needed to develop a processing technique that is not only reliable but is also created using materials that help in reducing the damage caused by the current processing techniques. It is estimated that the main components for battery production cost is divided over materials, labor and any overhead with processing technique, which accounts for approximately 80% of the total cost [16]. Therefore, the processing technique serves as a great avenue for reducing overall cost while also generating a positive impact on the environment. Apart from the financial aspects, there also exists an "environmental cost", which relates to the potential impact of the materials and process on the environment. Therefore, a process with high environmental cost may be characterized as being extremely harmful to the environment and personnel in direct contact with the materials needed for such a process. Therefore, research effort is needed in developing a possible electrode processing technique for LIBs that not only has a low environmental cost but also is cost-effective.

A typical LIB is composed of an anode, a cathode filled with electrolyte that acts as bridge to transport lithium ions between the two electrodes [13, 18, 19]. A typical anode is composed of a layer of graphite casted on a copper current collector. A typical cathode is composed of lithium-containing active material, carbon conductive additive, binder, and void spaces that are filled with the electrolyte, casted on an aluminum current collector. Since cathodes are the donors of lithium-ions during charging, they serve as a great research avenue for better materials but also for optimization of processing techniques [20-26]. The performance of a LIB is limited by several factors, one such being the capacity of the electrodes being used in the battery. Currently graphite is used a standard anode due to its stable performance and high abundance. Even though several research efforts have tried to move towards using higher capacity anode material, it worth noting that cathodes are the performance-limiting electrodes since, they dictate maximum operating voltage, thereby dictating the amount of lithium-ions extracted during charging. Therefore, as stated above, the cost associated with cathode production and its limiting characteristics make this a valuable area of research endeavor. An approximate cost breakdown for the production of LIBs has been shown in Figure 1, which shows that manufacturing is a major contribution to the overall cost [27].

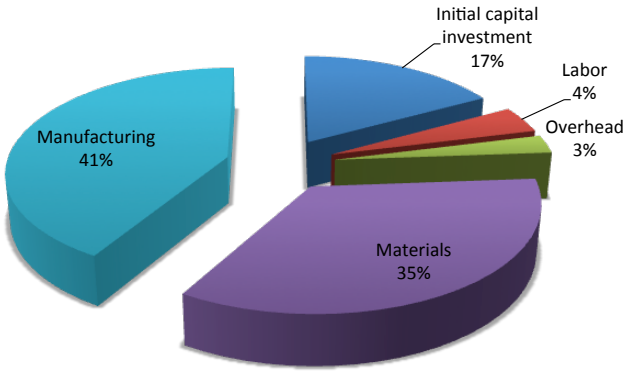

Figure 1: Cost breakdown for LIB production [28]

Standard LIB cathode processing is divided into the following sections: dry powder mixing, binder solution preparation, wet mixing, substrate preparation, film application and drying. Typically, wet mixing involves the use of organic solvent, like N-Methyl-2-pyrrolidone (NMP), such that this type of processing is commonly known as Organic or Non-Aqueous Processing. In Organic Processing, the binder of choice is usually Polyvinylidene fluoride (PVDF) mixed in NMP [29, 30]. This organic binder creates a homogenously dispersed mixture in the organic solvent. The use of NMP is not only restricted to LIB electrode processing as it is used extensively in other industries as a constituent chemical for paint and coating removal, petrochemical processing and industrial cleaning. Since NMP is a chemical that has a wide range of applications, it becomes very easy for humans and the environment to come in contact with this deadly chemical. It has been shown in various animal and human studies that NMP can penetrate the skin very readily, leading to reproductive toxicity in animals [31-35].

NMP has the potential to enter the environment as emissions into the atmosphere, since this volatile substance is commonly used a solvent, or through the industrial waste into the municipal water supply. It may not be well known but NMP has been qualitatively detected in drinking water supplies in the US since 1984 and was identified as a leachate in landfills in 1991 [36, 37]. It is estimated that in 1996, approximately 71,000 workers were exposed to NMP, while approximately 2.7 million consumers might have been exposed to it due wide range of application areas [38]. Currently, NMP is produced using gamma-butyrolactone and monomethylamine at temperate ranging from 150˚C – 310˚C [39, 40]. This process requires a significant energy and cost input, while maintaining high levels of process control to ensure that harmful by-products are properly handled.

According to the "The Safe Drinking Water and Toxic Enforcement Act of 1986", NMP has been identified as a chemical having the potential to cause cancer and reproductive toxicity [41]. It has been shown to cause delayed growth in offspring, damage to the nervous system due to long-term effects, irritation in the eyes, nose and throat, and may damage the liver. Controlled exposure of NMP in animals have shown fetotoxic effects to doses that may have no affect on the mother's health, leading to stillbirth of offspring [42, 43]. According to the WHO, NMP has very rapid dermal penetrations, thus causing severe irritation to the skin. Therefore, personnel that are exposed to NMP may have rapid dermal penetration of NMP, causing skin irritation, reproductive toxicity and cancer [44, 45]. Even though NMP is harmful to the environment and human life, there is an ever-increasing production due to its widespread

use in LIB electrode production. However, the effects of NMP do provide an inspiration to move away from such a harmful solvent that cause health damage to the personnel exposed to it but also to the environment in its creation and eventual disposal.

Since NMP is harmful to the environment and human health, there is a need to move away from the organic solvent towards using an omnipresent solvent such as, water as a suitable replacement for the production of LIB electrodes. Typically, when NMP is purchased in large quantities, it costs at least $2.25/L as compared to Deionized water (DI water) that costs approximately $0.015/L [27, 32]. The cost to purchase and produce deionized water is significantly lower and with the correct processing technique could serve as a potential replacement for the harmful NMP [46-50].

	Organic Processing	Aqueous Processing
Solvent	N-Methyl-2-pyrrolidone (NMP)	Deionized (DI) water
Health effects upon exposure	Hazardous	-
Approximate cost	NMP - $1.25/L	DI water - $0.015/L
	Binder - $8.6-10.5/lb	Water-soluble binder - $0.22-0.63/lb

Table 2: Comparison between Organic and Aqueous Processing for LIB electrodes

There has been some research effort into using deionized water as a possible replacement for NMP, thereby naming it as Aqueous Processing [16, 27, 28, 32, 46]. While using deionized water seems to be an attractive offer both in terms of environmental impact and cost, it does come with its own range of challenges, which has hampered development efforts in this area. PVDF does not mix in water due to its non-polar nature [46, 51, 52], therefore, water-soluble binders need to be used, such as Xanthan Gum (XG) or Carboxymethyl cellulose (CMC) [28, 32, 46, 53-55]. Even though water-soluble binders are being used, one must also understand the effects of surface tension that come into play with the solvent and substrate. Aluminum is known to be extremely hydrophobic, leading to formation of water beads, thereby preventing water to appropriately "wet" the surface. This implies that water cannot spread across the surface of the foil, which would severely limit the spreading of the cathode slurry on the aluminum current collector. However, Organic Processing does not face the same issue since surface tension of water (72.8 mN/m) is higher as compared to NMP (41 mN/m) at 25˚C [32]. Some research efforts in the area of Aqueous Processing have been shown that the aqueous slurry can be casted and dried on aluminum current collector. However, these processing techniques are not cost-effective and require highly specialized equipment. Corona discharge was used to increase the surface energy of the aluminum foil to allow for better wettability and subsequent on the current collector. This process uses highly energized ions, which bombard the surface of the foil and result in an increase in surface energy [16, 28, 32, 46, 56, 57]. The use of this pre-treatment step not only adds an additional step to the overall process but also requires the use of

expensive and specialized equipment since these machines can $50,000 or more according to online vendors. Therefore, the aim of this study is to combat the wettability issues that aqueous slurries will encounter without the use of any additional pre-treatment. Additionally, another hindering issue observed in Aqueous Processing is the agglomeration of active material when water is used to create slurries. This agglomeration is witnessed due to interactions between colloidal particles, due to hydrogen bonding and strong electrostatic forces. An active material such as Lithium Ferrophosphate is extremely small in size with a large surface area, these agglomeration effects become very evident in Aqueous Processing [16, 27, 28, 32, 46]. Therefore, studies have been conducted to use a dispersant such as Polyethylenimine (PEI) to combat the problems with agglomeration [16, 27, 28, 32, 46]. PEI creates a layer of positive charge surrounding the active particle, which prevents them from being attracted towards each other and allows for the formation of an electrode with more structural homogeneity. Therefore, this study will also address the impact on performance and electrode structure based on the proposed Aqueous Processing technique.

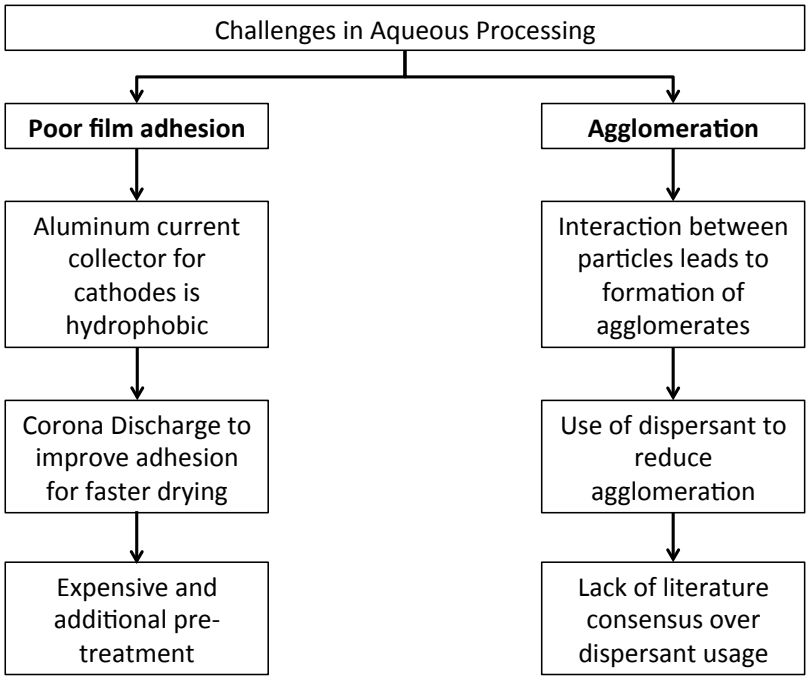

Figure 2: Challenges in Aqueous Processing

This study uses the standard ETSL Organic Processing as a basic for creating a technique for Aqueous Processing [58], so that it can be implemented without any additional pre-treatment or without the use of extra specialized equipment. In this study, Lithium Ferrophosphate ($LiFePO_4$) is used as active material due to its high theoretical capacity, excellent reversibility and thermal stability, which makes it a great contender for active material as a cathode in Lithium-Ion Battery [59-65]. Additionally, a 1-D model is also incorporated in this study to elucidate the results of this study. There are three physical effects that are observed during drying, evaporation of solvent, sedimentation and Brownian diffusion of particles in the solvent-based solution. In this

model, three non-dimensional numbers are defined that show relative influence of the above three physical effects - Peclet number, Sedimentation Peclet number and Sedimentation number that will be discussed in detail in the chapter related to the computational model.

CHAPTER II

AQUEOUS PROCESSING IN LIBS

Investigation of new processing techniques for Lithium-Ion Batteries in an academic environment can be conducted in several forms, with the most basic being the coin cell. Coin cells have become very popular and serve as one of the smallest form factors for the evaluation of new electrode materials and processing techniques. This chapter will provide an in-depth view into the processing technique and electrochemical performance results for LIBs created using Aqueous Processing.

Experimental Equipment

A typical LIB is composed of a cathode and an anode casted on aluminum and copper respectively, and filled with electrolyte as shown in Figure 3.

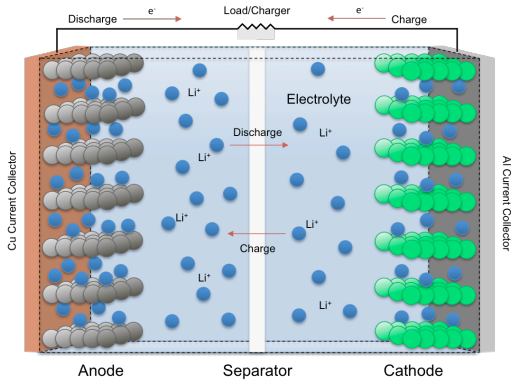

Figure 3: Schematic of a Lithium-Ion Battery

This study focuses on creating a processing technique for fabricating the cathode of a LIB, which is composed of active material, conductive additive and binder with void spaces that are filled with electrolyte. Cathode electrode fabrication using Aqueous Processing can be divided into six overall steps – substrate preparation, binder solution preparation, dry powder mixing, wet mixing, casting and thin film drying as illustrated in Figure 4.

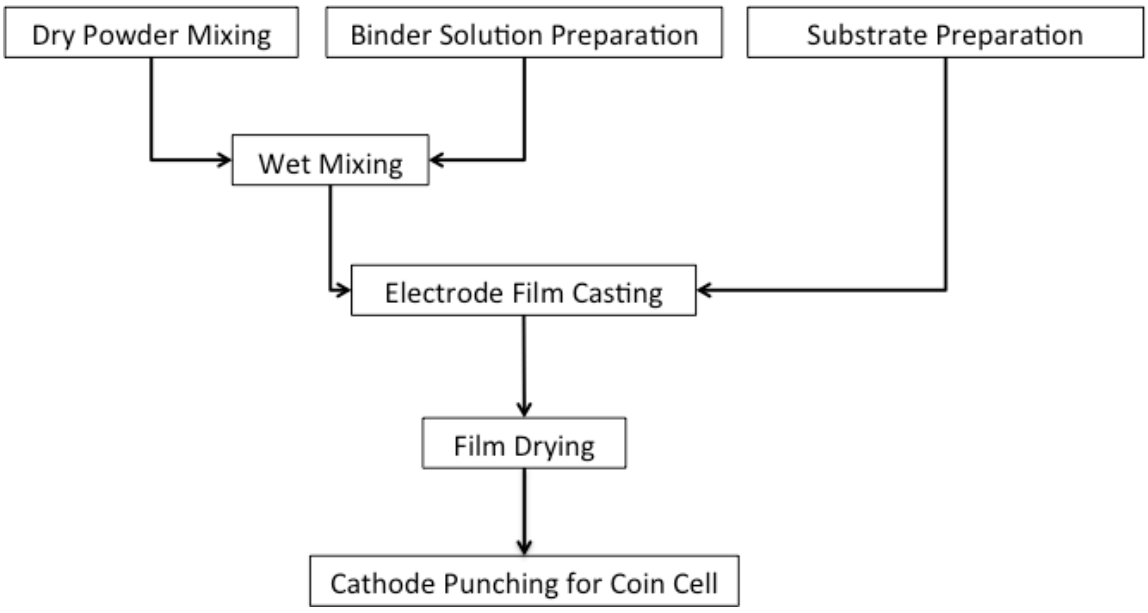

Figure 4: Schematic overview of the steps utilized for Aqueous Processing

A typical LIB cathode is casted on an aluminum current collector, which aids in the transport of electrons to the external circuit. The Swingline SmartCut Paper Cutter is used to cut a piece of aluminum foil upon which the cathode slurry will be casted and

eventually dry as seen in Figure 5. The aluminum foil is mechanically etched using a Scour Pad to remove a thin oil film that prevents adhesion between two layers upon rolling. This step is important to remove impurities as well as roughen the surface to promote adhesion of the slurry on the surface of the current collector.

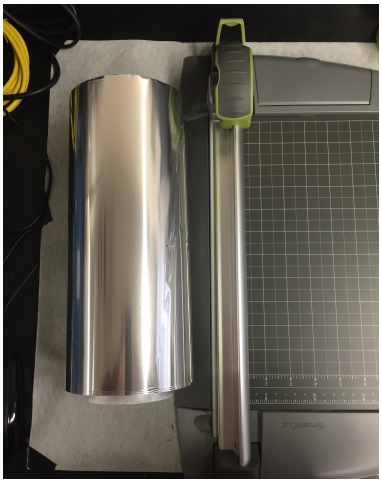

Figure 5: Aluminum foil and paper cutter

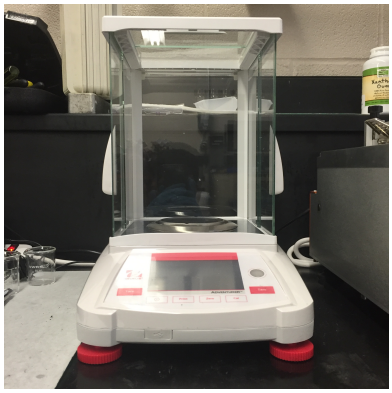

Figure 6: OHAUS Analytical Scale

The active material and conductive additive as weighed using an OHAUS Analytical Scale, which allows extremely precise measurements as shown in Figure 6. The OHAUS AX224/E has a readability of 0.1 mg, an accuracy of ± 0.2 mg and maximum capacity of 220 g. The dry powder mixing involves grinding the active material and conductive additive using a mortar and pestle. This breaks-up any clumps that the materials have formed, which allows in the creation of homogenized slurry. The materials used in this study along with the mortar and pestle used for dry mixing Figure 7.

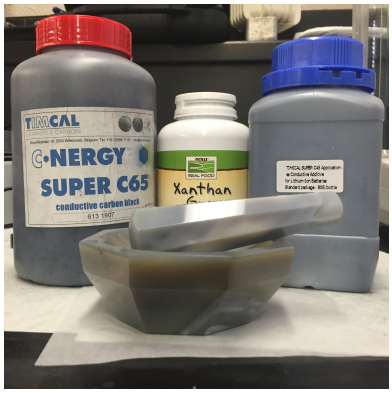

Figure 7: Powdered materials with mortar and pestle

This study also explores the effect of adding a dispersant in the slurry to prevent agglomeration of LFP particles [16]. Therefore the study will expand upon the modified mixing procedure in the later section of this chapter. Generally, the wet mixing stage is

subdivided into 2 stages – creation of binder solution and final wet mixing with dry powders. The binder solution can be created using a magnetic stirrer over a period of 72 hours or in an IKA mixing tube over a period of 3 hours. The two mixing equipment are shown in Figure 8 and Figure 9.

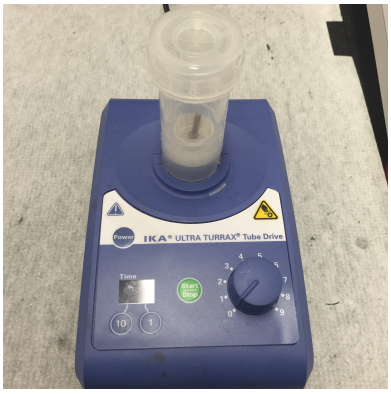

Figure 8: IKA tube mixing platform

Figure 9: Magnetic mixing platform

The slurry is then casted on the aluminum current collector using the Elcometer 4340 Automatic Film Applicator shown below in Figure 10. A doctor blade traverses over the foil, pushing the slurry at a constant speed and desired casting height to create a film of uniform thickness with 11 preset traverse speeds from 0.5 – 10 cm per second. The casted sheet is dried inside a MTI Vacuum Oven DZF-6020-FP with a temperature range of 50 – 250 ˚C with a pressure range of -0.1 MPa ~ 0 MPa (atmospheric pressure) as shown in shown in Figure 11.

Figure 10: Elcometer for casting films

Figure 11: MTI oven

Once the sheet has dried, a circular cathode is punched out using a hole punch as shown in Figure 12. The punched cathode is weighed and then transferred to a glovebox (Figure 13) for final coin cell assembly, which a pure argon environment with levels of O_2 and H_2O maintained below 0.5 ppm at all times. A crimper (Figure 14) is used to seal the coin cells assembled inside the glovebox.

Figure 12: Hole punch

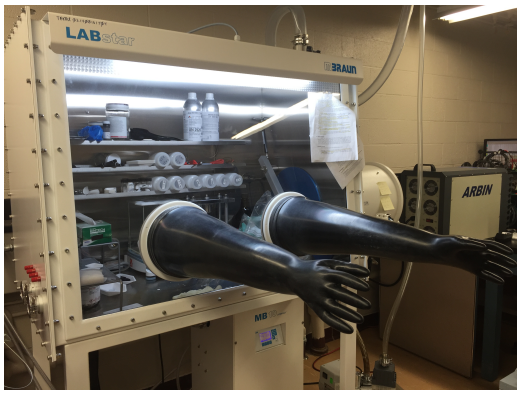

Figure 13: Glovebox

Figure 14: Crimper in the glovebox

After the coin cells have been assembled and sealed, they are electrochemically characterized via the usage of Arbin BT2000 and MTI BST8-MA systems as shown in Figure 15 and Figure 16. The MTI system can apply a current in the range of 0.02 mA – 10 mA with an accuracy of ± 0.1%. Its acquisition system can read with an accuracy of the ± 0.05%. The machine can operate between 0.5 V – 5 V with an accuracy of ± 0.1% and acquisition accuracy of ± 0.05%. The Arbin system has low current channels that are capable of applying current in the range of ± 100 μA with an accuracy of 0.1% of full range, with a voltage range of -10 V – 10 V.

Figure 15: Arbin BT2000

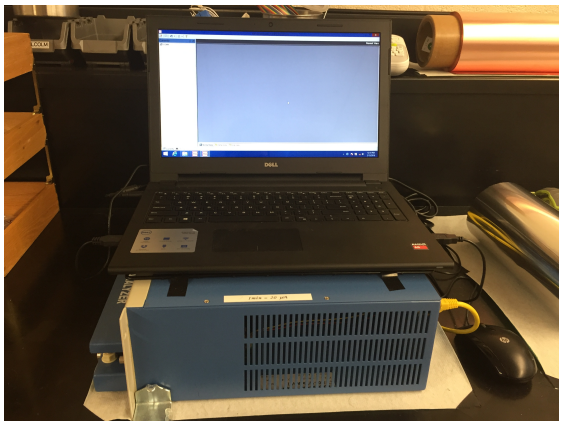

Figure 16: MTI BST8-MA

Materials

$LiFePO_4$ (LFP) with an average particle diameter of 0.75 µm, BET surface area of approximately 16 m^2/g and density of 3.6 g/cm^3 was acquired from MTI Corporation. Super C65 (carbon black) was added as a conductive additive with an aggregate size < 1 µm, BET surface area of 62 m^2/g and tap density of 0.16 g/cm^3 acquired from TIMCAL. Kynar Flex 2801 PVDF was supplied by Arkema, 1.0 M $LiPF_6$ in EC:DEC (1:1 by volume) was purchased from BASF and lithium ribbon was obtained from Sigma-Aldrich. Anhydrous N-methyl-2-pyrrolidone (NMP) was acquired from Sigma-Aldrich and DI water was acquired from the DI water supply line for the Doherty building on the Texas A&M campus, College Station.

Cathode and Coin Cell Preparation

The first step in the preparation of the cathode sheet requires the cleaning of the aluminum current collector, which will be the substrate upon which the slurry shall be casted. A 4.5" × 12" aluminum foil is cut by using the Swingline SmartCut Paper Cutter. When aluminum foil is obtained from the manufacturer, there exists a thin layer of grease between layers that prevents the foil to stick with itself. Therefore, the foil needs to be cleaned and etched to remove any grease in order to ensure good adhesion. The "dull" side of the aluminum foil is used for casting as it has less grease, thereby making it easier to clean without damaging the foil. The "dull" side (casting side) is laid face side up on a Teflon board with both surfaces covered with acetone. A Scotch Brite Scour Pad is used to mechanically etch the foil to create a rough surface for better film adhesion. The pad is used in circular motions during scrubbing while traversing side-to-side. Special care needs to be taken to ensure that the surface is not being over-scrubbed, which may cause the appearance of deep scratches. These deep scratches will create valleys around them, thus creating localized areas of poor slurry coverage and film adhesion. Spray more acetone on the scrubbed surface and wipe with a paper towel before moving to the non-casting surface or the "bright" surface and repeat the same operations as described above. Once both surfaces have been scrubbed, first rinse the casting side with DI water and repeat it on the non-casting side. While cleaning the surfaces with DI water, ensure that there is no noticeable beading of water; otherwise the surfaces need to be scrubbed again to remove any oil residue. Clean the non-casting side with Isopropyl Alcohol (IPA) and repeat the same on the casting side. Place the "wet"

foil between two paper towels and firmly press to remove any water. The foil is then allowed to dry for 30 minutes between two papers towel under paperweights to remove any water that wasn't removed in the earlier step.

The binder solution can be created either using the magnetic stirrer method or by using an IKA mixer as mentioned previously. Weigh the desired mass of binder (Xanthan Gum) and solvent (DI water) to a 330 mL plastic bottle, which will use a magnetic stirrer to create a homogenized solution over a span of 72 hours. In this study, weigh 0.1 g of Xanthan Gum (XG) and add 14.5 g of DI Water (DI water) to a 330 mL plastic bottle with a magnetic stirrer. This leads to 1:145 ratio of XG:DI water , or approximately 0.68% of XG in DI water.

The next stage is the dry powder mixing of the active material and the carbon conductive additive. In this study, the desired composition of the dried electrode is to be 80% LFP, 10% Super C-65, and 10% XG by mass. Weigh out 0.2736 g of LFP and 0.0342 g of Super C-65 into a mortar and pestle. During the dry mixing stage, a mortar and pestle are used to grind the powders together to break any lumps that may exist. This ensures that the active material and conductive additive are uniformly mixed prior to wet mixing. Perform this operation for approximately 5 minutes until the mixture looks uniform and devoid of any lumps. This mixture of dry powders is then transferred to a 20 mL IKA tube for the final stage of wet mixing with the binder solution. Add the correct amount of binder solution to ensure that the 80:10:10 wt % composition is maintained. Add 16 glass balls (6 mm in diameter) to the IKA tube. Place the IKA tube

on the mixing platform and ensure that the glass balls are moving around and bouncing off the top of the cap to achieve adequate mixing.

Polyethylenimine (PEI) is a dispersant that creates a layer of positive charge surrounding the LFP particles. This prevents LFP particles form being attracted towards each other and allows for a uniform casting leading to a cathode with greater surface homogeneity. In order to create a binder solution with PEI, choose the overall composition of PEI relative to other dry powders. For example, the overall composition can have 8% XG and 2% PEI with 80% LFP and 10% C65 by dried mass. Since PEI is a viscous liquid, it will be created along with the binder solution in the same mixing vessel. Branched PEI was used in this study, which is soluble in water under high-shear mixing. Weigh out the correct mass of PEI, XG and corresponding mass of DI water required to create the PEI and binder solution. First weigh out PEI and DI water in a 20 mL IKA tube and allow mixing for 1 hour. Since branched PEI is soluble in water; a clear solution will be obtained. Weigh out the amount of XG into the previously mentioned IKA tube and allow mixing for 2 hours to create a white solution as shown in Figure 17. This binder and dispersant solution can be used for the wet mixing stage with the active material and conductive additive. Once the final wet mixing stage is complete, a black slurry is produced as shown in Figure 18. The slurry should be visually examined to check for consistency, as the slurry should neither look too dilute or thick. If the slurry is very dilute, it will spread over a wide area when casted and wont cast properly if very thick.

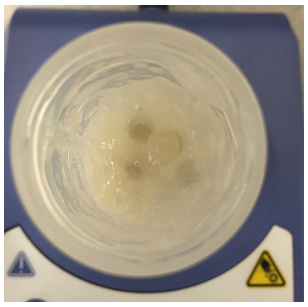

Figure 17: PEI, XG and DI water solution (top view)

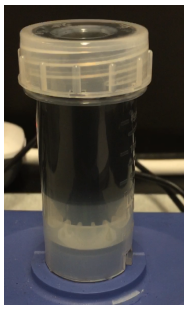

Figure 18: Final electrode slurry

The final electrode slurry is now ready to be casted on the cleaned aluminum foil. Before the slurry can be casted, the surface of the Elcometer Film Applicator and the Doctor Blade will be cleaned with IPA and wiped with a paper towel. Spray IPA on the Elcometer before transferring the dried aluminum sheet to ensure that the sheet adheres to the surface. Ensure that the "dull" side or casting side is face up and use a paper towel to press the surface to flatten and remove any excess IPA from below the foil. Transfer the contents of the slurry on the prepared aluminum foil. In this study, the Doctor Blade was set to 8 mils (~200 μm) with a speed level of 3 (20 mm/sec) to ensure uniform casting of the sheet as shown in Figure 19. The sheets were dried in a MTI oven at 50˚C for approximately 8 hours as seen in Figure 20.

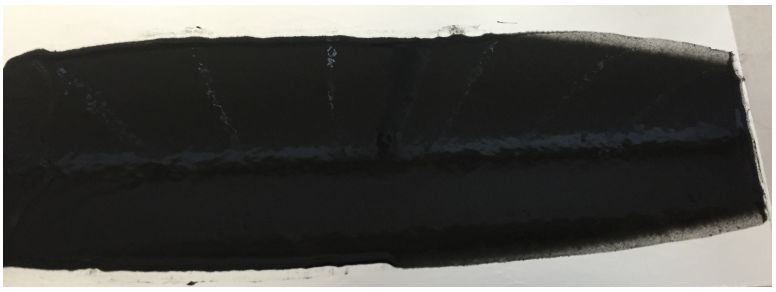

Figure 19: Casted cathode sheet

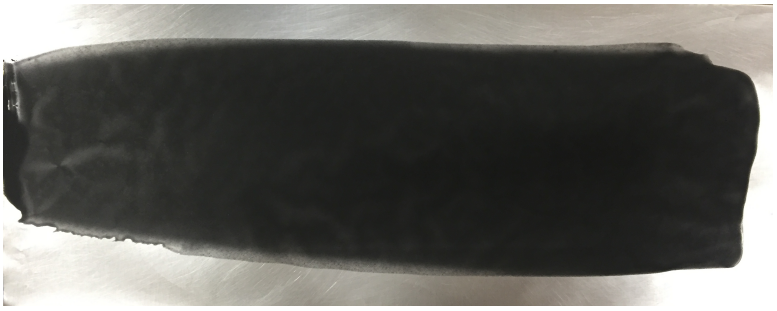

Figure 20: Dried cathode sheet

Use a hole punch to punch out 0.5” diameter cathodes from the sheet and weigh them on the OHAUS scale as seen in Figure 21. A special note needs to be taken into account while punching cathodes from the electrode sheet to examine adhesion. A poor sheet adhesion will lead to flaking and breakage of the dried slurry. In this study, a qualitative measure of adhesion is taken into account such that when a cathode is punched, a sheet with good adhesion will not flake. A quantitative measurement of adhesion can be performed by peel tests or specialized equipment that would measure horizontal and vertical forces required to scrape the film [66-70]. The punched cathodes

are weighed to estimate the applied current during electrochemical characterization, as it will be discussed in the later sections of this chapter.

Figure 21: Electrode sheet shown with punched cathode

Transfer these cathodes to a 20 mL glass vial and into the antechamber of the glove box. Once the glove box has been purged to remove any outside air with argon, open the inside latch of the antechamber. A typical coin half-cell consists of the following components- coin cell case, cathode, Celgard separator, gasket, anode on a metallic spacer, a wave spring and a coin cell cap as shown in Figure 22.

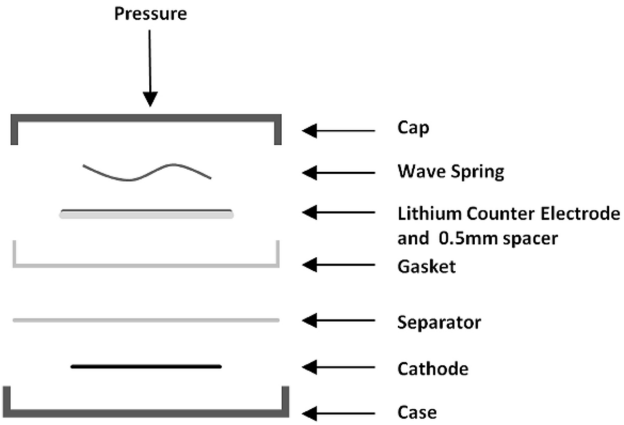

Figure 22: Coin cell components displayed in order of placement within cell [58]

In this study, only half-cells were fabricated such that the lithium metal served as the anode instead of graphite (on a copper collector) for a typical full cell. This lithium-counter electrode is adhered onto a 0.5 mm metallic spacer, serving as the anode. The lithium metal, serving as the counter-electrode, is always placed inside the glovebox to prevent oxidation, which can be visually observed as the "blackening" of the metal. Even though the environment inside the glove box is maintained at less than 0.5 ppm of O_2, lithium might still get oxidized. In order to use lithium metal in the coin cell, it has to be cleaned to remove the oxidized lithium and roughen the surface to allow for adhesion with the metallic spacer. The lithium ribbon can be cleaned with a razor blade on both sides before it is ready to be used in the coin cell. Punch a 0.5 mm circular piece of lithium metal and firmly press the lithium metal to the 0.5 mm spacer.

In order to start the cell assembly, place the metal case in a weight boat where the final assembly will take place. The cathode is placed in the middle with the electrode

side up (aluminum side down) in the case and approximately 3 drops of the electrolyte ($LiPF_6$ in EC: DEC) are added on to the surface of the cathode. The $^3/_4$" separator is placed on top of the cathode, which is a semi-permeable membrane that allows only lithium-ions to transport between the electrodes through the electrolyte. Care must be taken when placing the separator on the cathode, as this step is prone to the introduction of air bubbles. If air bubbles are present, use a pair of plastic tweezers to gently push the air bubbles from under the separator. If the electrode moves out of the center, gently grab the case by the tip and tap to force the electrode to be centered again. Place a gasket inside the cell case and add approximately 3 drops of electrolyte on the separator film. The gasket is placed to ensure that the case and the cap of the cell don't touch each other in order to avoid the cell from internal short-circuiting. The anode is composed of lithium metal attached to a 0.5 mm spacer with the lithium face down. A wave spring is placed on the spacer to protect the internal components from crushing upon crimping. Several drops of electrolyte are then added to ensure the system is flooded with electrolyte. The coin cell cap is placed on top and pushed down by the operator. The cell is then transferred to the crimper using tweezers, where approximately 800 psi of pressure is applied to seal the cell.

After the cell has been crimped, it is ready to begin cycling for electrochemical characterization and the cells are subjected to cycling between 2.5 – 4.2 V at several C-rates. C-rate is a standard that is used to determine the current and time required for the cell to either charge or discharge between the necessary operating voltages. Therefore, at a C-rate of 1C, the applied current will charge (or discharge) the cell in 1 hour (3600

seconds). Hence, a C-rate of C/20 would apply $^{1}/_{20}$ th of the current for charging (or discharging) over 20 hours. The theoretical specific capacity of LFP is approximately 170 mAh/g [29]. Therefore, in order to determine the current associated with a C-rate, it is important to know the theoretical specific capacity and the amount of active material in the punched cathode. With the weigh of an average $^{1}/_{2}$" foil, the amount of active material can be determined by subtracting the mass of the foil from the overall electrode mass and multiplying it with the percentage of active material based on the composition. After acquiring this number, the cells can be cycled in using MTI's Battery Analyzer station and Arbin BT2000 system as seen in the equipment section of this chapter under Figure 15 and Figure 16.

Results and Discussion

The proposed processing technique was developed through a series of steps that involved; creating a baseline performance with in-house Organic Processing using LFP, creating a composition using DI water and xanthan gum, and adding PEI to previous processing with DI water and xanthan gum. In order for a direct comparison between Organic and Aqueous Processing, several electrochemical tests were conducted to obtain a baseline for cells created using Organic Processing. The theoretical specific capacity of LFP is approximately 170 mAh/g [29]. A composition of 80:10:10 wt % (active material: conductive additive: binder) with LFP, C65 and PVDF was casted on a 4.5" × 12' aluminum foil and dried at 50˚C. In order to create a baseline for Organic Processing, the cells were cycled at a low rate of C/20. At lower C-rates, the flux of

electrons reaching the active material in the cathode to combine with the lithium-ions is very low, such that the cell is operating very close to its Open Circuit Potential (OCP). This would allow the battery to lithiate and de-lithiate the maximum amount of lithium possible. C-rates lower than C/20 can also be performed by as C-rate decreases; the time to charge (or discharge) also increases, along with possible plateau in performance. Hence, C/20 was chosen due to time and performance capability of the testing equipment since C/20 was very close to the least count of the equipment.

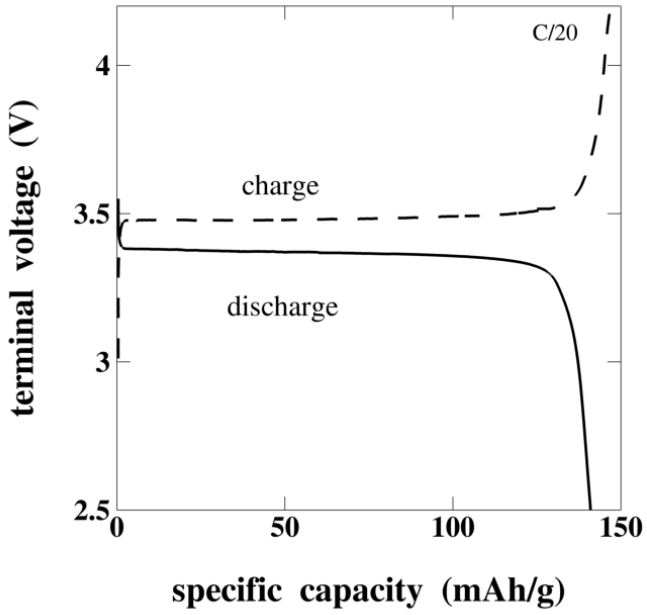

Figure 23: Representative baseline performance of in-house Organic Processing

At very low C, lithium have more time to delithiate (or lithiate) into the bulk of the active material during charging (or discharging), which leads to a higher achievable reversible capacity. This allows for maximum amount of lithium and providing the maximum possible capacity. Cycling at low C-rates of C/20, C/10 and C/5, provided a working baseline of the in-house Organic Processing. Tests at C/5, C/2 and 1C were also performed to obtain performance curves and trends. As current increases, it leads to a higher concentration gradient of lithium-ion at the surface of the active material. Due to this high flux, but very slow lithiation process, a very small set of lithium can reversibly lithiate and delithiate, causing a reduction in achievable reversible capacity as current increases [29, 32]. The performance data for all the cells created using Organic Processing cycled at various C-rates can be seen below in Figure 24. The data shown in the figure below is the average performance per C-rate. Approximately 5 coin cells were created from this electrode sheet and cycled at the above-mentioned C-rates. The obtained performance data was plotted against SOC and C-rate. SOC is defined as the obtained reversible capacity normalized against the maximum reversible capacity. Each error bar indicates the deviation from the average of approximately 1 standard deviation.

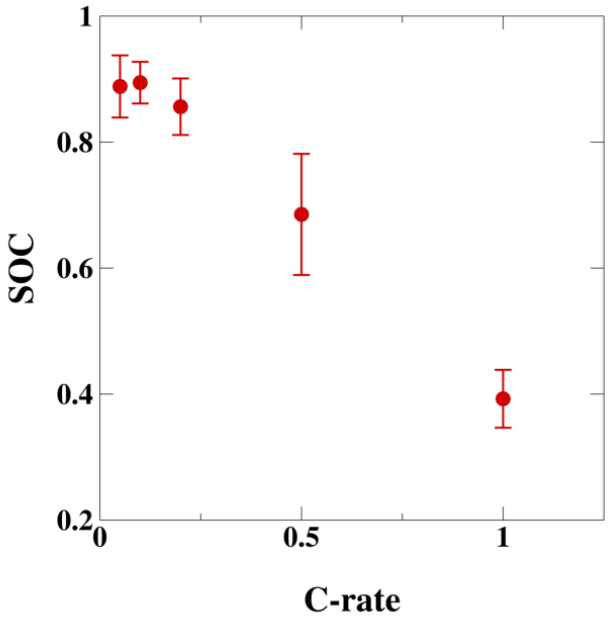

Figure 24: Performance of cells fabricated using Organic Processing

The charge and discharge curves for a representative cell created using Organic Processing composition can be seen in Figure 25. These are very typical discharge curves for a material like LFP, where during discharge a constant voltage is observed due to the material properties. This occurs due to the lithium-ions combining at the surface of the active material, while creating an interface that moves, allowing more lithiation of lithium into the bulk of the active material.

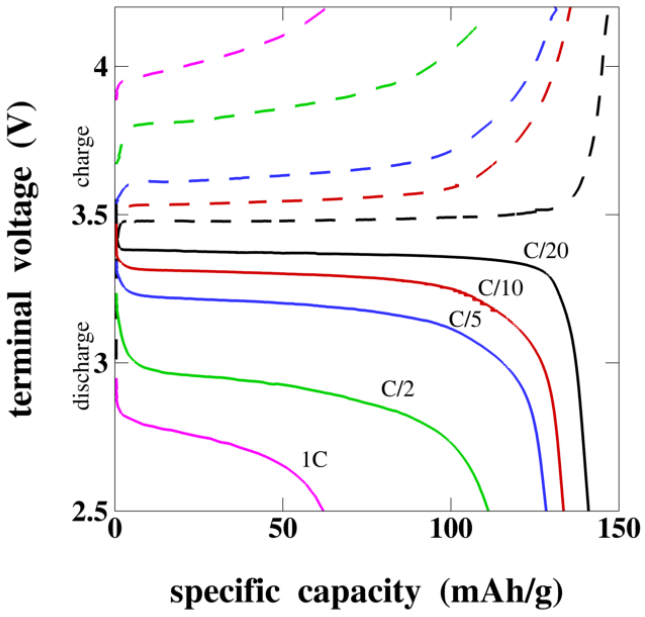

Figure 25: Charge and discharge curves for a representative cell prepared using Organic Processing

Multiple cells were created from the 80:10:10 wt % composition and the data obtained is statistically significant with 36 data points (an average of 5 points at each C-rate). The variation in performance could be due to possible human errors during processing and assembling, along with any controller issues with the Data Acquisition System of the MTI Battery Analyzer.

In order to confirm the behavior of obtaining approximately 140 mAh/g at low C-rates, cells from a different composition were subjected to electrochemical testing. Therefore, a composition of 70:20:10 wt % (active material: conductive additive: binder) was casted on 4.5" × 12" aluminum and dried at 50˚C. The cells assembled from this

cathode sheet were cycled at the same C-rates for comparison. It was observed that changing the composition did not significantly change the performance and saturated at approximately 136 mAh/g. The cells made from the 70:20:10 wt % composition displays a similar level of performance and the same trend as its counterpart of 80:10:10 wt % composition. There is a slight difference between their performances at 1C, which can be attributed to the presence of more carbon additive in the cathode. The carbon additive provides pathways for electrons to travel inside the cathode and combine with the lithium-ions at the surface of the active material, which eventually leads to the lithiation inside the active material. Therefore, by adding more carbon additive by mass, leads to less ohmic drop, which creates a longer lasting region of constant voltage but ultimately results in lower obtainable reversible capacity. This is possibly due to more coverage of active material by carbon additives, leading to lower surface area for electrochemical reaction. Therefore, it can be concluded to be no change in the maximum achievable specific capacity of the material using the in-house Organic Processing with the 70:20:10 wt % as seen in Figure 26. However, if the mass percentage of active material is increased at the expense of carbon additives and binder, then it is possible to introduce challenges in film adhesion or higher ohmic losses due to less electronic conductive pathways. Therefore, it can be seen from the above reported data that the in-house Organic Processing can serve as a viable baseline for performance comparison with Aqueous Processing.

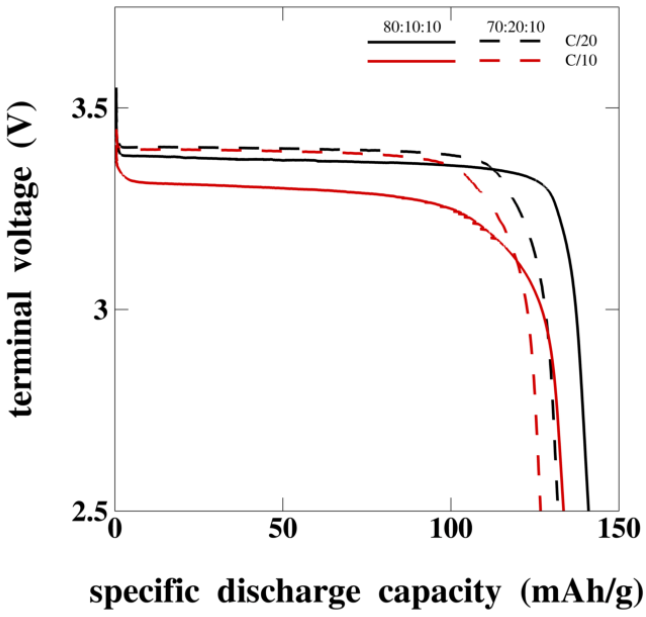

Figure 26: Performance comparison of 80:10:10 wt % and 70:20:10 wt % (Organic Processing)

Electrode sheets were fabricated using the proposed Aqueous Processing technique to examine electrochemical performance. A composition of 80:10:10 wt % (active material: conductive additive: binder) with LFP, C65 and XG was casted on a 4.5" × 12" aluminum foil and dried at 50˚C. A cell produced from Aqueous Processing was cycled at C/20 to compare with the baseline performance from Organic Processing as shown in Figure 27.

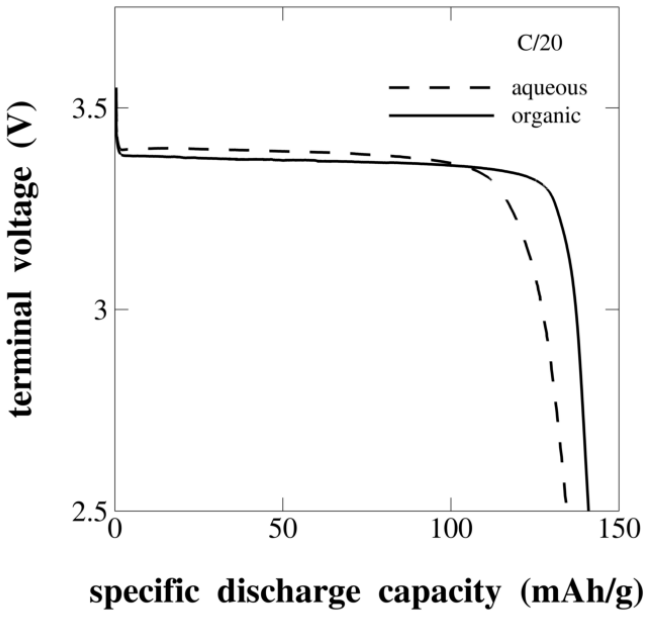

Figure 27: Baseline comparison between Aqueous and Organic Processing

Approximately 9 cells fabricated from several aqueous electrode sheets and were cycled at various C-rates of C/20, C/10, C/5, C/2 and 1C to determine the trends in performance. Composite data from these 9 cells results in similar trends in performance over different C-rates, produced under the same processing technique, with the same composition and same drying temperature. The obtained performance data was plotted against SOC and C-rate. SOC is defined as the obtained reversible capacity normalized against the maximum reversible capacity. Each error bar indicates the deviation from the mean performance of all the cells cycled with a magnitude of 1 standard deviation.

The data obtained from cycling cells created using Aqueous Processing show a similar trend as seen before, where low C-rates have better reversible capacity that high C-rates. This is due to the lower flux of electrons at low C-rates that allows for more lithium-ions to combine with the electrons at the surface of the active material along with more intercalated lithium.

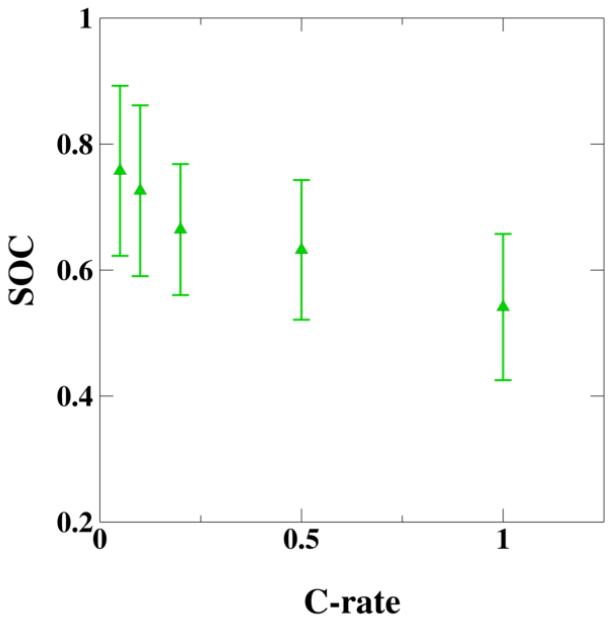

Figure 28: Performance of cells created using Aqueous Processing

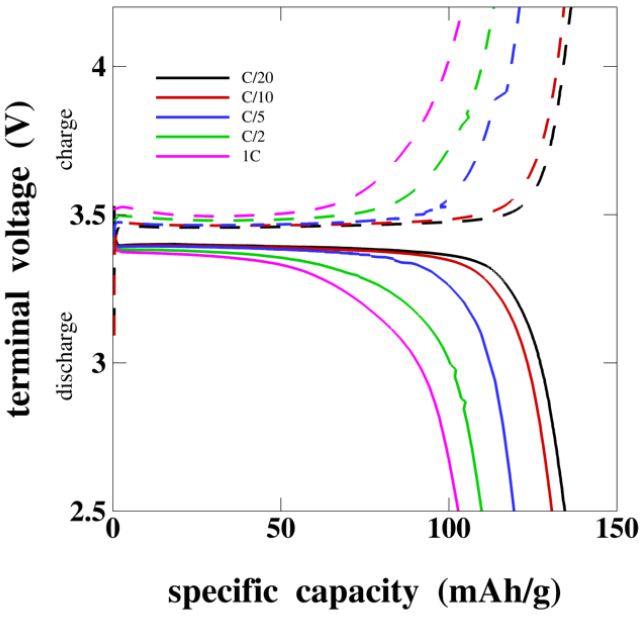

Figure 29: Charge and discharge curve for a representative cell prepared using Aqueous Processing

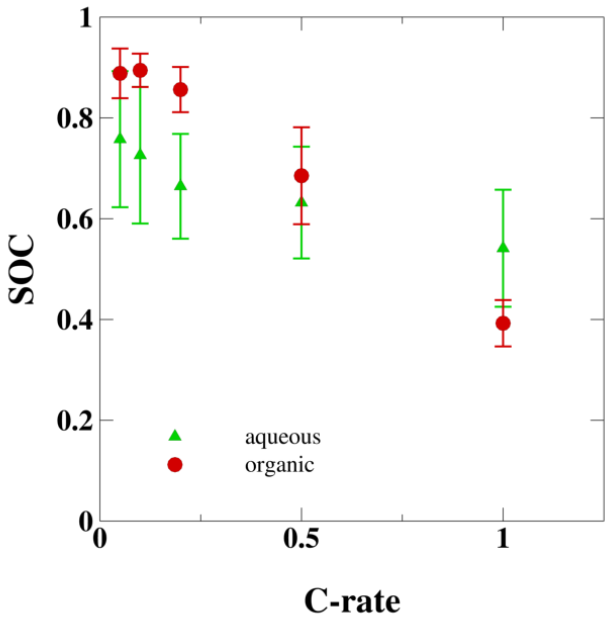

Figure 30: Performance comparison between cells prepared using Organic and Aqueous Processing

Therefore, the data does seem to suggest that the in-house Organic and Aqueous Processing technique, using the same active material and conductive additive give comparable performances over several C-rates as shown in Figure 30. However, it should be noted that there is a wide spread in the obtainable reversible capacity of the cells created using Aqueous Processing. This scattered performance may be due to agglomeration and a non-uniform cathode structure that is created upon drying, which may be due to higher evaporation rate of water when compared to NMP at 50˚C.

As shown earlier, evaporation of the solvent for both Aqueous and Organic Processing, seem to have a discernable impact on the obtainable reversible capacity of fabricated cells. Therefore, the effect of drying temperature was also investigated for Aqueous Processing in this study. This was performed for two primary reasons – understand the effect of evaporation on electrode structure and performance along with a further decrease in the overall processing cost. Therefore, electrode sheets were dried at 70˚C, 30˚C and in laboratory ambient conditions with a recorded temperature of 21˚C ± 1.5˚C. The electrode sheets took approximately 6 hours to dry 70˚C, approximately 9 hours to dry at 30˚C and approximately 13 hours to dry at ambient drying conditions. It must be stated that when the electrodes sheets were dried at ambient conditions (21˚C ± 1.5˚C), it implies that the electrode sheets were allowed to dry in the ETSL lab outside a vacuum oven in the ambient environment. This drying temperature was selected to see if the proposed Aqueous Processing could be conducted at ambient drying temperature, without the use of an oven, thereby reducing the cost of processing even further as stated above.

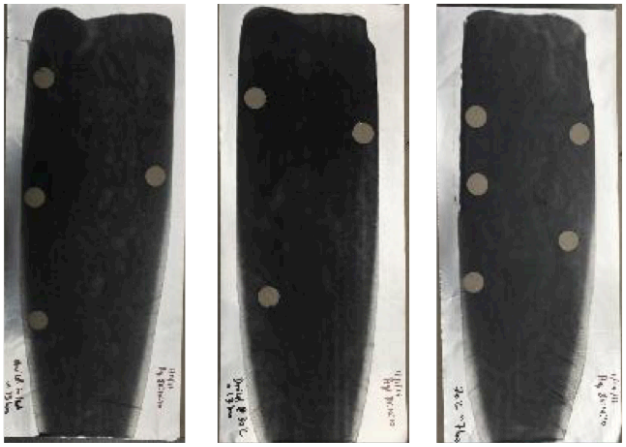

Figure 31: Cathode electrode sheets dried at different temperature (Aqueous Processing)

The cells prepared from the above 3 electrode sheets were cycled at C/5, C/2 and 1C and their comparative performance can be seen in Figure 32. Approximately 3 cells were fabricated from each electrode sheet and cycled several times at different times over the course of two weeks to obtain the data presented below. The data seems to suggest that a higher drying temperature is resulting in a higher obtainable reversible capacity, while comparing cell performance between Organic and Aqueous Processing. However, in the case of Aqueous Processing, cells created with an electrode sheet with a drying temperature of 70˚C, seem to be providing higher reversible capacity. The data also seems to suggest that cells created using electrode sheets that were dried at 30˚C are providing lower reversible capacity as shown in Figure 32. The data also seems to

indicate that there is a reversal in performance obtained by the cells created from the ambient dried sheet.

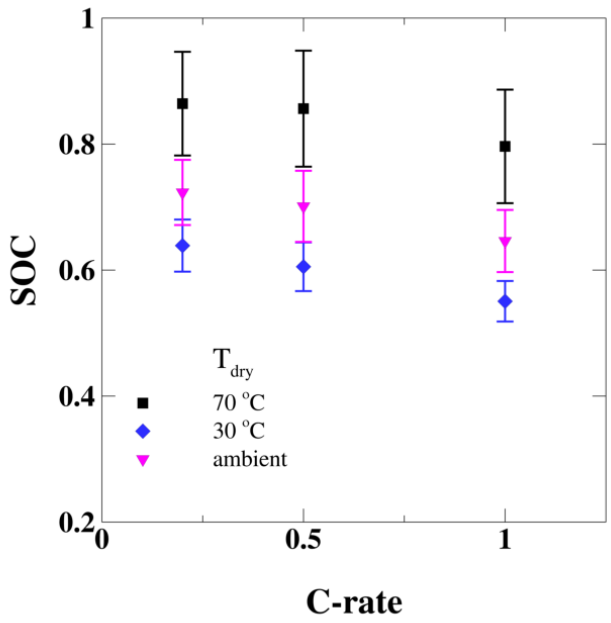

Figure 32: Performance comparison of cells prepared from electrode sheets dried at different temperatures (Aqueous Processing)

The cell with maximum performance for each case was chosen from each drying temperature condition of Aqueous Processing to analyze the charge and discharge curves as shown in Figure 33, Figure 34 and Figure 35. The performance curves for the 3 representative cases indicate the presence of two different competing physical phenomenon that are dictating the maximum obtainable reversible capacity.

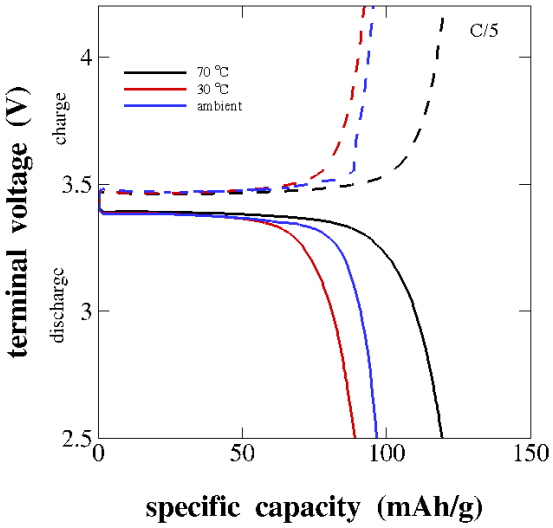

Figure 33: Charge and discharge curves for a cell from each electrode sheet cycled at C/5

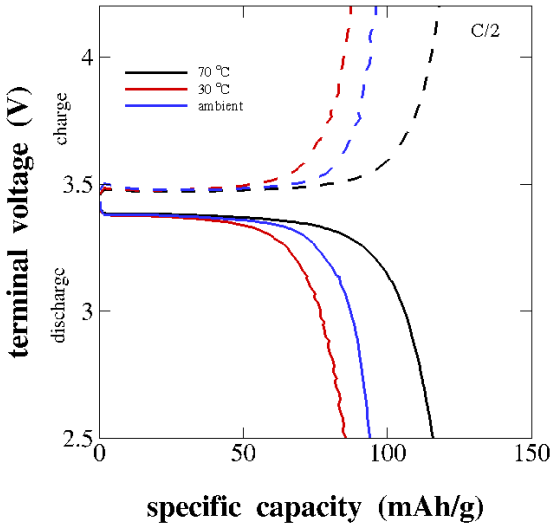

Figure 34: Charge and discharge curves for a cell from each electrode sheet cycled at C/2

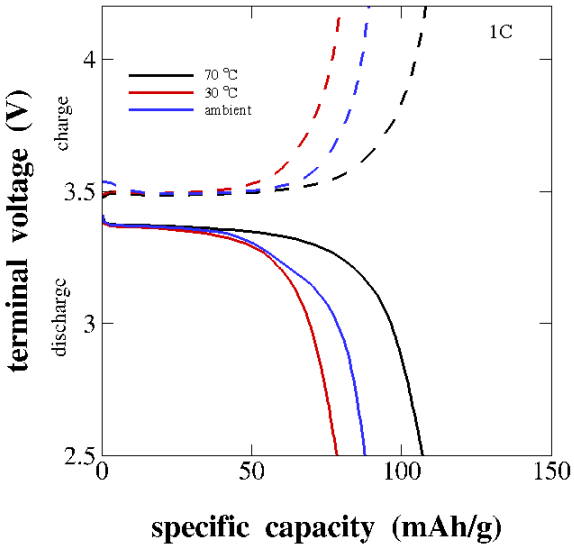

Figure 35: Charge and discharge curves for a cell from each electrode sheet cycled at 1C

There are two different physical effects at play in the above performance and charge-discharge curves. The slurry created using the wet stage mixing is composed of various particles that are homogenously dispersed. As this slurry is casted and allowed to dry, the particles that are suspended inside the slurry begin to sediment or diffuse to equalize any concentration gradients that might exist. As the drying temperature increases, the evaporation rate also increases. Hence, a sheet will dry faster at 70˚C as compared to drying at 50˚C. A high evaporation rate prevents the constituent particles to get enough time to sediment or diffuse (these processes are inherently very slow for the micron sized-particles). This allows the lighter particles like carbon to remain homogenously dispersed in the slurry and be surrounded by suspended carbon particles. This allows for electrons to have pathways to combine with the lithium-ions at the boundary of the active particles and a better performance than cells from a 50˚C dried sheet. Even though, the performance may have increased by increasing the temperature, there were several visible "pits" that were formed on this electrode sheet, which may be due to a high evaporation rate. Therefore, temperature higher than 70˚C were avoided since the visible "pits" would increase with temperature, leading to a non-uniform electrode.

However, the opposite was observed at lower temperatures when the performance data was analyzed. At lower drying temperatures, the evaporation rate is lower, and therefore, suspended particles will have more time to sediment or diffuse to equalize concentration gradient. This will also allow LFP particles to form agglomerates that will lead to a smaller surface area for lithiation, which may promote a lower

attainable reversible capacity. The formation of agglomerates also leads to a lower coverage of carbon particles around the active material. This further reduces the electronic conductivity inside the cathode, leading to a higher ohmic resistance and a faster drop in voltage, which results in a lower reversible capacity. Therefore, decreasing the drying temperature in the oven, leads to lower capacity.

However, there is a reversal in the observed performance from the cells fabricated using the ambient dried sheet. It is observed that the performance of cells from sheet dried at 30˚C is less than that cells obtained from sheet under ambient drying. This observed change in performance trend can be attributed to a reversal to change in drying conditions over the course of the drying period. It should be reiterated that the drying times and conditions between these three electrode sheets were different. Since ambient drying is prone to changes in Relative Humidity, air velocity over the drying sheet and other fluctuations that might be induced due to the external environment, it may be possible that the evaporation rate might have been impacted. This caused the reversal of the two physical effects discussed earlier, thereby creating a microstructure that leads to a better obtainable reversible capacity.

Therefore, the data does suggest that the proposed Aqueous Processing can be conducted at various drying temperature, such that drying at a high temperature of about 70˚C can lead a higher capacity at the cost of pit formation. However, a lower drying temperature of 30˚C leads to the formation of agglomerates, which increase ohmic resistance and causes a loss in reversible capacity. In the ambient drying conditions, external fluctuations can impact the net evaporation and hence the resulting electrode

and performance. In order to confirm the above trends, the cells were cycled at different operating temperatures.

Cells fabricated from the aqueous sheets dried at different temperatures were subjected to cycling at several ambient temperatures. This was performed to investigate the effect of operating temperature on reversible capacity. Higher temperatures will lead to higher diffusivity of lithium into (and out of) the active material, thereby providing more lithium-ions to transport between electrodes, allowing for higher reversible capacity. Cell created from the three sheets were cycled at 1C in a thermal chamber at several operating temperatures ranging from 5˚C to 45˚C in increments of 10˚C. As expected, the cells from the electrode sheet dried at 70˚C does seem to be providing more reversible capacity than its counterparts as shown below. The average performance of all cells from various electrode sheets can be seen in Figure 36 and the overall performance of cells from the 50˚C sheet can be seen along with the deviation.

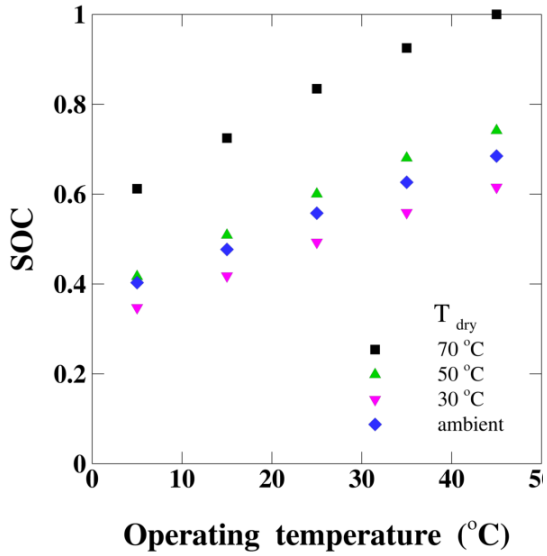

Figure 36: Average performance comparison of cells from different temperature dried electrode sheets under several operating conditions

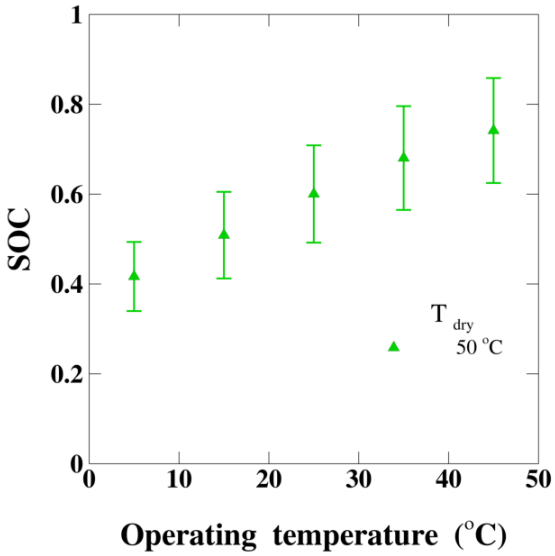

Figure 37: Performance of 3 cells prepared from an aqueous sheet dried at 50˚C

In order to visually examine the effect of evaporation rate on electrode formation, Back Scattering Emission (BSE) SEM images of electrodes were acquired to investigate the morphological features and establish trends that would also explain the observed electrochemical performance. In this study, a qualitative analysis is conducted based on what is observed visually. As shown earlier, cells created using Aqueous Processing have a comparable performance as compared to cells from Organic Processing across several C-rates. As it can be visually analyzed, the top surface of the electrode structure created using Organic Processing has more surface homogeneity due the low evaporation rate of NMP. This surface homogeneity leads to a lower development of

surface craters that has less surface topological variation. The absence of surface craters leads to improves carbon coverage, leads to high available surface area for lithiation, thereby leading to a higher obtainable reversible capacity as seen before in the experimentally.

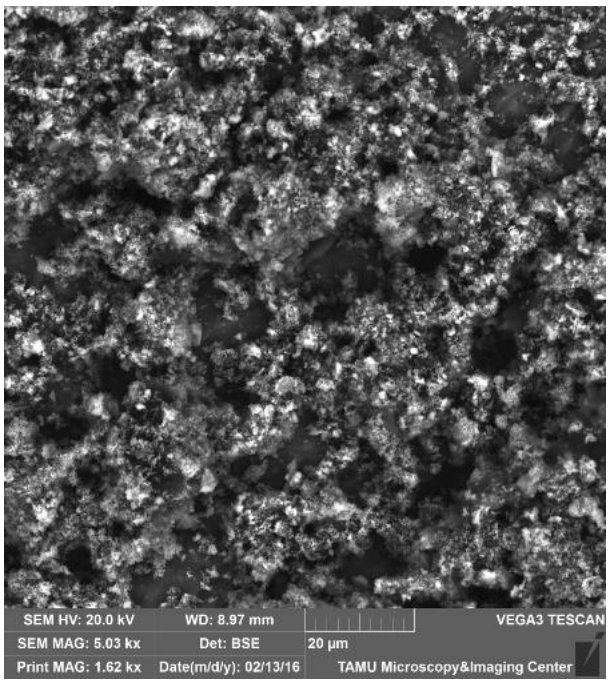

Figure 38: Aqueous Processing at 50˚C

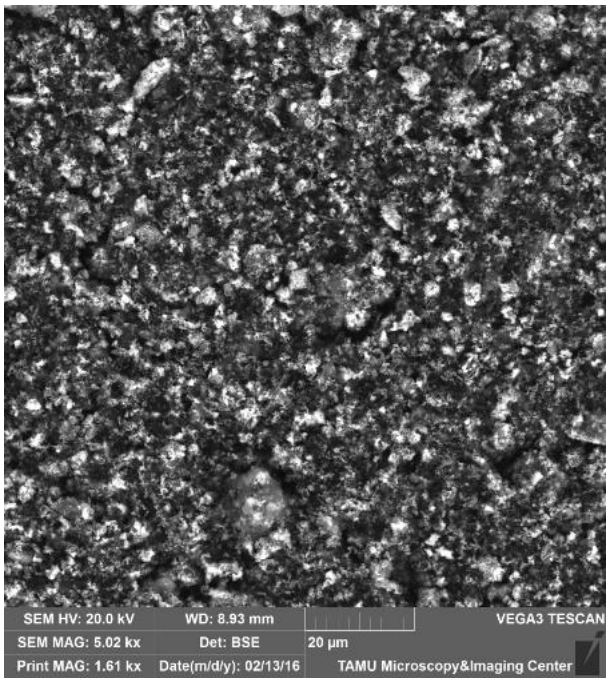

Figure 39: Organic Processing at 50˚C

Performance trends observed for Aqueous Processing can also be visually corroborated using SEM image of the top surface of the electrode for the various sheets. Electrode sheets dried at 70˚C, created using Aqueous Processing, consists of some areas with no material coverage, thereby creating surface craters. This may possibly be due to a higher evaporation rate of water at 70˚C as compared to 50˚C. The SEM images in Figure 38 and Figure 40, corroborate that high evaporation rate is leading to the formation of "pits" and some areas with no material coverage. These surface craters lead to a low surface homogeneity, thereby creating an imbalance of material coverage, which may impact the overall performance. In the case of electrode sheets dried at 70˚C,

the cells were performing much better than their 50˚C counterparts. This could be associated with the high evaporation rate leading to less time for the particles to settle but leading to more coverage by suspended carbon particles. Since the slurry created during wet stage mixing is homogenously dispersed, a fast drying regime would not allow big particles, like the active material particles to settle down, thus allowing more particles to accumulate at the top of the electrode. Since carbon particles are much smaller in size, a fast drying is also coupled with a uniform dispersion of carbon particles that provide good coverage, leading to more conductive pathways, and hence higher reversible capacity.

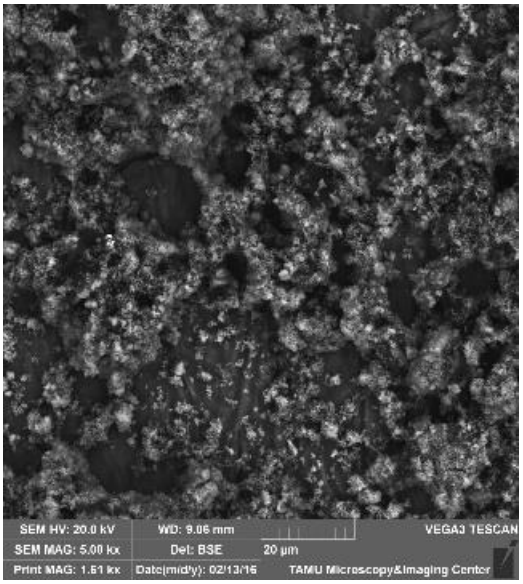

Figure 40: SEM image of a cathode dried at 70˚C

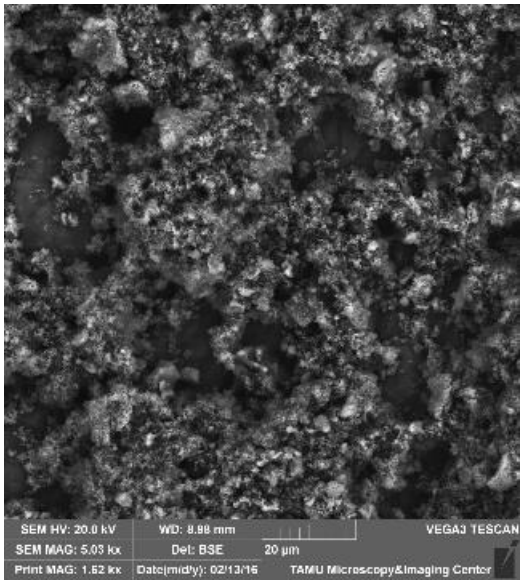

Figure 41: SEM image of a cathode from 30˚C

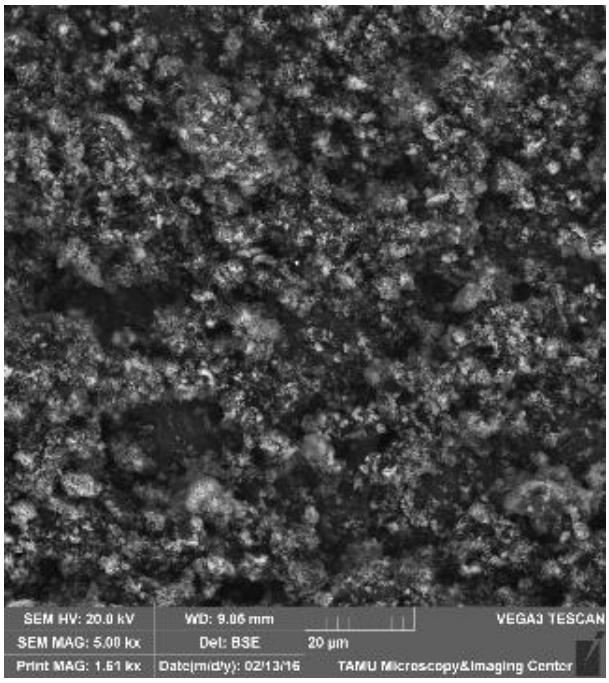

Figure 42: SEM image of a cathode from approximately 21˚C

However, at lower drying temperatures, evaporation rate decreases, which allows active material particles to settle down and create aggregates as seen in Figure 41 and Figure 42. The formation of large aggregates also leads to the formation of surface craters, leading to a low surface homogeneity. As seen in the SEM images and the previous performance curves, it is observed that lower evaporation rate is leading to formation of bigger "islands", which is leading to a higher surface area of active material for lithiation and de-lithiation. This is also leading to less coverage of carbon particles around the large agglomerates of active material, which increases the resistance experienced during cycling, leading to lower reversible capacity. However, a different

trend in performance is seen when cells from the ambient sheet are compared to cells from the 30˚C sheet. Even though the evaporation rate for 21˚C ± 1.5˚C sheet is lower than 30˚C, it must be reiterated that this sheet was dried in the lab facility and not inside a controlled environment. Even though the drying temperature is lower, the presence of external fluctuations like relative humidity or air movement can impact the overall process of drying, which is observed in the SEM images of the sample at ambient drying conditions. It is observed that the top of the electrode has fewer agglomerates with slightly less areas with less material coverage and hence higher surface homogeneity. This is indicative that there might have changes in the room, other than temperature, that could have impacted the drying process. In this study, the cells created from the ambient dried sheet seems to be performing better than 30˚C but this may not always be the case due to lack of a controlled environment. Therefore, this shows that the proposed Aqueous Processing can be conducted at a drying temperature of 21˚C ± 1.5˚C at ambient conditions, while having a comparable performance with its counterparts. However, since 21˚C ± 1.5˚C is not a controlled drying temperature, it is extremely difficult to predict performance, thereby this study will focus on the best possible temperature between 70˚C, 50˚C and 30˚C. Since cells from the 50˚C dried electrode sheet has the most "optimal" performance with the least non-uniformities, consequent studies will be performed at the drying temperature.

It has been shown that a lower drying temperature tends to the formation of "islands" of active material. This is observed since LFP particles tend to form agglomerates by the creation of attractive and repulsive potentials due to Van der Waals

forces [16, 32, 71]. Hence, a dispersant such as Polyethylenimine (PEI) is added to the slurry in order to reduce such attractive forces by creating a layer of positive charge around the LFP particles, causing repulsion and preventing the formation of agglomerates. However, the addition of an additive like PEI is not a standardized process therefore, this study aims at establishing a possible working window that could solve this issue.

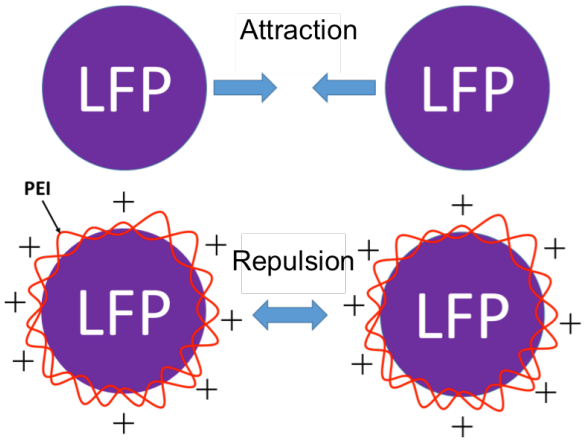

Figure 43: PEI creates a layer of positive charge around LFP to prevent agglomeration

A composition of 80% active material, 10% conductive additive and various combinations of binder and PEI were chosen for the remainder 10% by mass. The 4 combinations of XG:PEI were as follows – 9:1, 8:2, 7:3 and 6:4 wt % respectively. It has been studies that addition of PEI will reduce the size of agglomerates formed upon

drying, thereby promoting a cathode microstructure with higher homogeneity and providing a better performance with less unpredictability. In this study, the addition of PEI reduces the amount of binder being added, which compromises the adhesion of the film onto the sheet and can lead to an electrode sheet prone to flaking. This was evident when sheets created with 6% XG and 4% PEI by mass had poor casting, drying and adhesion as seen in Figure 44. The electrode sheet created using this composition has created a porous electrode with poor adhesion due to lower amount of binder.

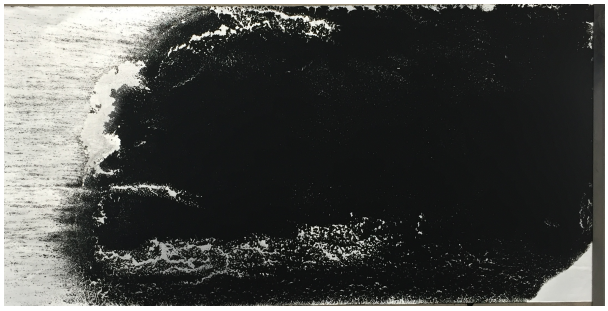

Figure 44: Aqueous sheet dried at 50˚C with 6% XG and 4% PEI by mass

Hence, no cells were prepared from this sheet and only sheets with the following XG:PEI were considered – 9:1, 8:2 and 7:3 wt % respectively.

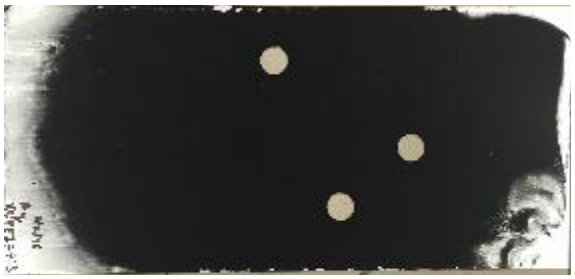

Figure 45: Aqueous sheet dried at 50˚C with 7% XG and 3% PEI by mass

Figure 46: Aqueous sheet dried at 50˚C with 8% XG and 2% PEI by mass

Figure 47: Aqueous sheet dried at 50˚C with 9% XG and 1% PEI by mass

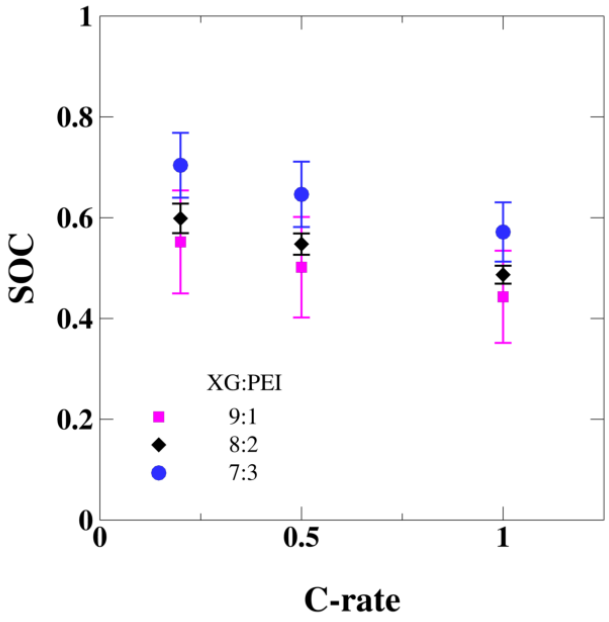

Figure 48: Performance comparison between cells with various binder and dispersant concentrations

There were 3 electrodes created from each sheet and cycled four times at C/5, C/2 and 1C during different times in a 3-week period. It should be noted that only the composition was changed however, the other steps of the processing technique were kept the same. The data seems to suggest that cells from the sheet with a composition of XG:PEI of 8:2 by mass provides a consistent performance across all C-rates tested in this study. This is expected since addition of PEI is a tradeoff between reducing particle agglomeration, film adhesion and material coverage. The cells from the sheet with a composition XG:PEI of 9:1 by mass is “closer” to our earlier baseline aqueous sheet as seen previously. It is expected that this composition will have bigger agglomerates due

to a lower contribution of PEI. This would lead to the formation of bigger agglomerates than its other XG:PEI counterparts, which would lead into a lower surface homogeneity and hence we will get a large variation in obtainable reversible capacity.

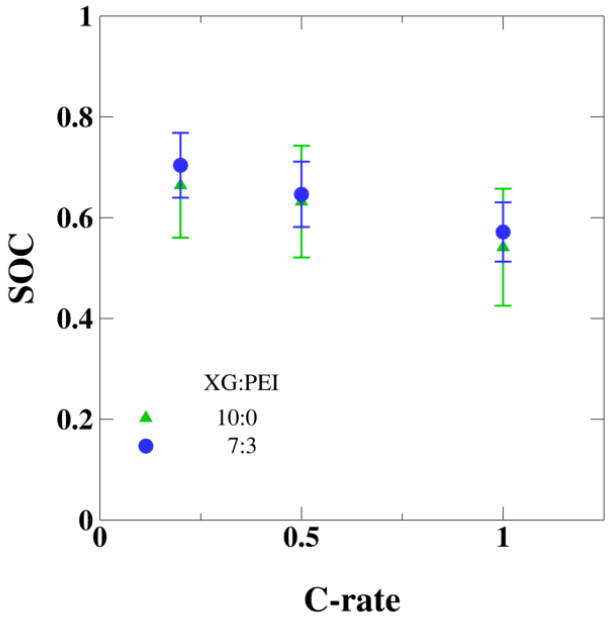

Figure 49: Performance comparison between no PEI (10:0 wt %) and 3-wt % PEI (7:3)

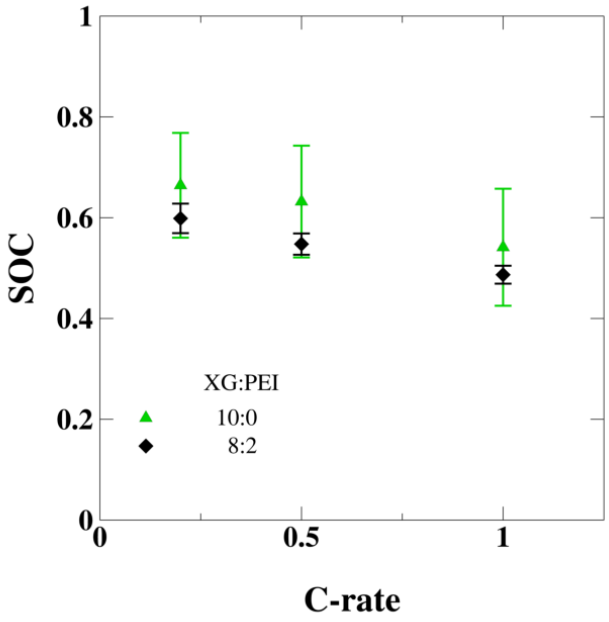

Figure 50: Performance comparison between no PEI (10:0 wt %) and 2-wt % PEI (8:2 wt %)

As expected, electrodes from the sheet with a composition of XG:PEI of 7:3 is expected to contain smaller agglomerates, which might lead to an electrode with higher surface homogeneity. However, with less binder in the composition as compared to its counterparts, there may be areas with less material coverage, thereby leading to a performance with a larger variation with the formation of surface craters. It must be noted that the PEI was added to the overall composition to reduce particle agglomeration, such that it would lead to a higher surface homogeneity. However, the cells prepared from the intermediate case of XG:PEI of 8:2, leads to a better tradeoff in terms of material coverage and smaller agglomerates. The observed variation in performance and surface topology can be confirmed with the BSE SEM images shown

below. The SEM images below showcase the non-uniform surface topology as discussed above.

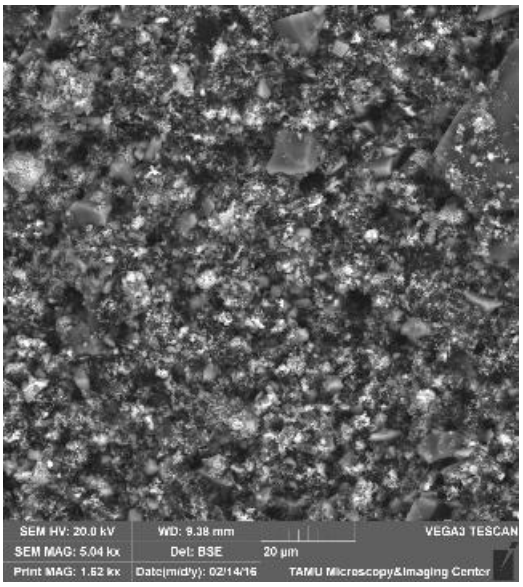

Figure 51: SEM image with 9% XG and 1% PEI by mass

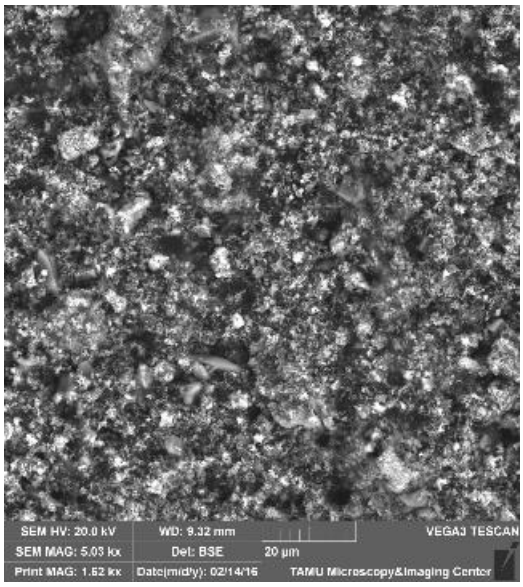

Figure 52: SEM image with 8% XG and 2% PEI by mass

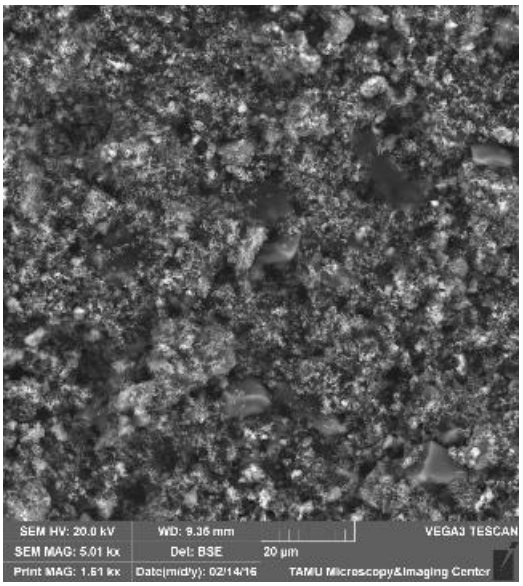

Figure 53: SEM image with 7% XG and 3% PEI by mass

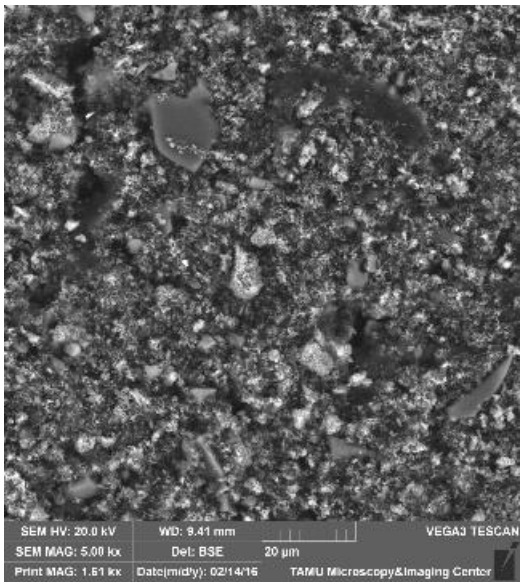

Figure 54: SEM image with 6% XG and 4% PEI by mass

Therefore it can be seen from the proposed processing technique a fine balance between drying temperature, particle agglomeration and adhesion has to be taken into consideration. It was shown that the most "optimal" drying temperature with "optimal" performance is 50˚C since it leads to the formation of an electrode with high surface homogeneity along with the less "pits" and smaller agglomerates as compared to 70˚C or 30˚C. It was also shown that in order to decrease the agglomeration formation, PEI must be added to the composition. As seen from the data presented above, it can be concluded that for the proposed processing technique, a composition of 80:10:8:2 wt % (active material: conductive additive: binder: dispersant) leads to a reduction in agglomerate size, high surface homogeneity, low surface craters with the most optimal performance.

CHAPTER III

PHYSICS OF ELECTRODE DRYING

It was shown in the earlier section, that the drying temperature has an effect on the final microstructure and consequently on its performance. Given a basic understanding of the drying dynamics, a simplified 1-D model was used to elucidate the macroscopic observations. Casted slurry goes through two stages during drying – evaporation of the solvent and compression of the constituent particles once enough solvent has evaporated as seen in Figure 55.

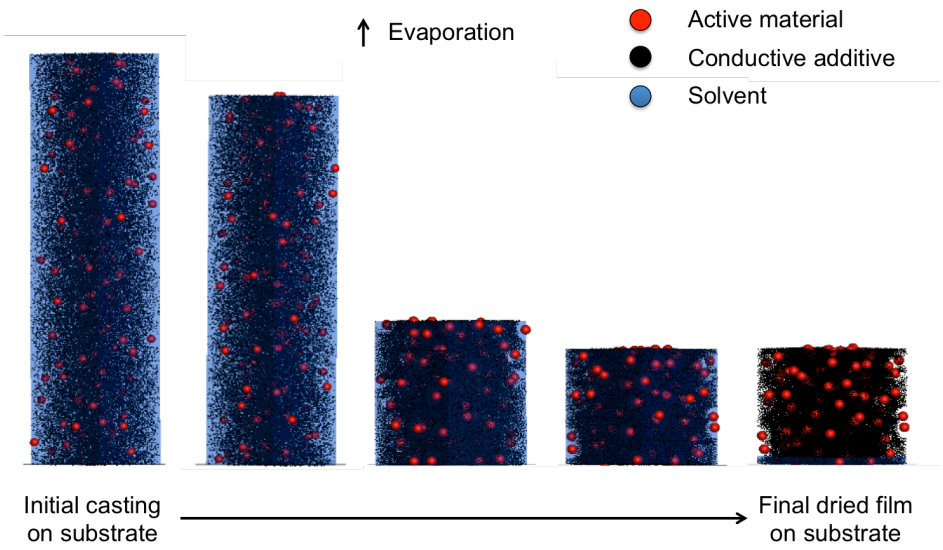

Figure 55: Progression of slurry drying and film formation

The active material is depicted as red spheres, the black spheres represent the carbon additives and the background color represents the binder in the solvent. The top surface recedes due to evaporation, which causes the binder and additive to accumulate at the solution-substrate interface. The final cathode microstructure is formed during the drying phase of the electrode manufacturing; hence it plays a very significant role in the overall performance of the cell [10, 11]. The electrode microstructure is an important aspect that dictates the performance of the LIB since it provides information on how the constituent particles are distributed. An electrode with a high cross-section and surface homogeneity will lead to the optimal performance as it was shown in the previous section. Therefore, to understand the variation of properties inside the electrode and obtain optimum performance it is necessary to study the drying process. In this study, a 1D-drying model is used to elucidate the observations of drying temperatures on the distribution of active particles after drying.

Model

There are three physical effects that are observed during drying, evaporation of solvent, sedimentation and Brownian diffusion of particles in the solvent-based solution. Evaporation causes movement of particles from the top of the coating towards the surface of the substrate. Sedimentation originates when particles try to settle down due to gravity of their own mass. Brownian diffusion of particles tries to counteract the gradient of particles of formed between the layers of the coating. These affect particle distribution, such that their net effect creates the final electrode microstructure.

Therefore, a combined understanding of these effects is important to elucidate the drying patterns observed previously for Aqueous Processing.

In the previous section, it was shown that the slurry casted on the aluminum foil consists of active material, conductive additive and binder mixed in a solvent, thereby creating a 4-phase system that needs to be taken into account during drying. However, in this study, the conductive additive and binder are smaller in size as compared to the active material; such that diffusion is dominate for these species. Hence, their volume fraction can be assumed to be constant over the entire domain, thereby creating a single phase in which active particles get arranged.

The 1-D equation for the LFP particle is based on the diffusion, sedimentation and evaporation, and is given as [72-74]:

$$\frac{\partial \phi}{\partial t} = \frac{\partial}{\partial z}\left(U\phi + D\frac{\partial \phi}{\partial z} \right) \tag{3.1}$$

where U(Φ) is the sedimentation velocity and D(Φ) is the diffusion coefficient. There is a no-flux boundary condition that is applied to the substrate-slurry interface, such that

$$y = 0,\ U\phi + D\frac{\partial \phi}{\partial y} = 0 \tag{3.2}$$

However, there exists an effective flux at the slurry-air interface, where evaporation is happening, such that is causes a decrease in slurry height over time, as follows

$$y = H_0 - Et\ ,\ U\phi + D\frac{\partial \phi}{\partial y} = E\phi \tag{3.3}$$

In the above equations, H_0 is the initial casting thickness, E is the evaporation rate in terms of rate of change in height, D is the particle diffusion coefficient and U is the particulate sedimentation velocity. As mentioned earlier, the combined effects of evaporation, sedimentation and diffusion have to be taken into account to understand the final arrangement of the active particles in the electrode microstructure. These physical effects occur at 3 different timescales, such as –

$$t_{diff} \approx \frac{H_0^{\,2}}{D_0} \tag{3.4}$$

$$t_{evap} \approx \frac{H_0}{E} \tag{3.5}$$

$$t_{sed} \approx \frac{H_0}{U_0} \tag{3.6}$$

In order to understand the relative importance of these effects, a non-dimensional Peclet number will be defined [72-74]. Peclet number for evaporation is defined as the rate of evaporation versus the rate of diffusion of particles and is given by

$$Pe = \frac{EH_0}{D_0} \tag{3.7}$$

where, D_0 is Stokes-Einstein diffusion coefficient, defined as:

$$D_0 = \frac{kT}{6\pi\mu R} \tag{3.8}$$

where, R is the radius of the spherical particle in a liquid with viscosity μ at a temperature T, H_0 is the initial film height thickness, k is the Boltzmann constant, and E is the rate of evaporation (in terms of rate of change in height). If during the drying process, evaporation is dominating, then Pe >> 1, whereas for diffusion dominated

systems, Pe << 1. In an evaporation dominant drying regime, the particles are densely packed at the solution-air interface, leading to a higher material accumulation top (solution-air interface) versus the bottom (solution-substrate interface). However, for diffusion dominated systems, the particles will move within the film to equalize any concentration gradients that will try to create a vertically uniform electrode microstructure.

A Peclet number for sedimentation and evaporation was also defined as the relative strength between the two processes, and is given by

$$Pe_{sed} = \frac{H_0 U_0}{D_0} \tag{3.9}$$

where D_0 is Stokes-Einstein diffusion coefficient as defined previously. In the above expression, U_0 is defined as the Stokes settling velocity of a spherical particles and is given by

$$U_0 = \frac{2R^2 g(\rho_p - \rho_s)}{9\mu_s} \tag{3.10}$$

where R is the radius of the spherical particle, g is the gravitational acceleration, ρ_p is density of the particles, ρ_s is the density of the solvent and μ_s is the viscosity of the solvent.

Using the above non-dimensional numbers, we can further develop another relation that compares sedimentation with respect to evaporation, known as the sedimentation number N_s and defined as

$$N_s = \frac{U_0}{E} = \frac{Pe_{sed}}{Pe} \tag{3.11}$$

Therefore, when $N_s >> 1$, it implies that sedimentation is the dominant, which would allow more particles to settle down and may lead to a higher accumulation at the solution-substrate interface. However, if $N_s << 1$, evaporation is dominant, implying that particles will have less time to settle, leading to a higher accumulation at the solution-air interface.

In this study, $LiFePO_4$ (LFP) particles were modeled to predict the evolution of volume fraction across the height of the casted slurry as it dries. Since only the volume fraction of active material is being modeled, the properties of conductive additive and binder have to taken into account along with those of the solvent. Therefore, in order to treat the solvent as a single-phase system, effective density and viscosity had to be calculated to account for the carbon particles and binder as follows:

$$\rho = \rho_a \beta + \rho_s (1-\beta) \tag{3.12}$$

$$\mu = \frac{\mu_s}{(1-\beta)^{2.5}} \tag{3.13}$$

$$\beta = \frac{\alpha}{1-\phi} \tag{3.14}$$

where β is the volume fraction of the carbon black particles and binder mixed in solvent and LFP particles, α is the volume fraction of the carbon black particles and binder when only pure solvent is present; ϕ is the volume fraction of LFP particles. Therefore, as the solvent evaporates, the volume fraction of the active material decreases, which leads to a higher contribution of conductive and binder particles to the effective density and viscosity, making the film more viscous, as one would observe in reality.

As the casted slurry dries, there is a change in the overall height of the slurry. Therefore, the height in the vertical direction continues to decrease over time due to evaporation, leading to change in domain during drying. Hence, the time and height was non-dimensionlized, such that it leads to the expressions below

$$\bar{t} = \frac{t}{H_0 / E} \tag{3.15}$$

$$\bar{y} = \frac{y}{H_0} \tag{3.16}$$

This leads to non-dimensionalization of the governing equations and boundary conditions

$$\frac{\partial \phi}{\partial \bar{t}} = \frac{\partial}{\partial \bar{z}} \left(N_s A(\phi, \beta) U_0 \phi + \frac{1}{Pe} B(\phi, \beta) D_0 \frac{\partial \phi}{\partial \bar{z}} \right) \tag{3.17}$$

$$y = 0,$$

$$N_s A(\phi, \beta) U_0 \phi + \frac{1}{Pe} B(\phi, \beta) D_0 \frac{\partial \phi}{\partial \bar{z}} = 0 \tag{3.18}$$

$$\bar{y} = 1 - \bar{t}$$

$$N_s A(\phi, \beta) U_0 \phi + \frac{1}{Pe} B(\phi, \beta) D_0 \frac{\partial \phi}{\partial \bar{z}} = \phi \tag{3.19}$$

Since the upper boundary (slurry-air interface) is continuously decreasing, a time independent coordinate was used as follows

$$\xi = \frac{1}{1 - \bar{t}} \tag{3.20}$$

$$\tau = \bar{t} \tag{3.21}$$

After incorporating the above time independent coordinate system, the final governing equation and boundary conditions are as follows

$$\frac{\partial \phi}{\partial \tau}+\frac{\xi}{1-\tau}\frac{\partial \phi}{\partial \xi}=\frac{N_s}{1-\tau}\frac{\partial}{\partial \xi}(A\phi)+\frac{1}{Pe(1-\tau)^2}\frac{\partial}{\partial \xi}\left(B\frac{\partial \phi}{\partial \xi}\right) \tag{3.22}$$

$$\xi = 0$$

$$N_s A\phi+\frac{1}{Pe(1-\tau)}B\frac{\partial \phi}{\partial \xi}=0 \tag{3.23}$$

$$\xi = 1$$

$$N_s A\phi+\frac{1}{Pe(1-\tau)}B\frac{\partial \phi}{\partial \xi}=\phi \tag{3.24}$$

In the above equations, A(Φ,β) and B(Φ,β) are defined as

$$A(\phi,\beta)=(1-\phi)^{6.55}(1-\beta)^{2.5}\left(1-\beta\left(\frac{\rho_a-\rho_s}{\rho_p-\rho_s}\right)\right) \tag{3.25}$$

$$B(\phi,\beta)=\left[(1-\phi)^{6.55}\frac{\phi_m}{(\phi_m-\phi)^2}(1-\beta)^{2.5}\right] \tag{3.26}$$

As the process of drying reaches its completion, it results in the decrease in height of the top layer by reducing the upper limit of y/H_0. At $\bar{t}=1$, the sheet will be fully dried, but the upper limit of maximum possible packing fraction prevents from reaching normalized time to 1. This is due to the random closed packing leading to the solid objects having the maximum volume fraction. Since the active particles are assumed to be hard spheres, the maximum closed packing density achievable is approximately 0.64, and loose packing density of 0.4, which become the stopping criteria for the model [72-78]. Therefore, this prevents us to fully "dry" the sheet, but

allows for a prediction of the distribution of particles based upon the longest possible drying time achievable.

Results and Discussion

The model in this study only provides a qualitative measure of the particle distribution. The drying model in this study is validated against the model developed by Cardinal et. al [72], as shown in Figure 56 and Figure 57. In this cases below, Peclet number and Sedimentation numbers, show two different cases. In one case, where Peclet number equal to 10, the casted slurry is in a drying regime where the evaporation rate is dominant. This leads to more material to remain suspended on the top surface of the casted slurry, which is pushed down as the solvent evaporates. This creates a large gradient in the amount of active material present at the top of the overall dried film. However, in the case where both Peclet and Sedimentation numbers are the same, it creates a situation where diffusion, sedimentation and evaporation are all equally dominant. This leads to a gradual concentration gradient that tends to be approximately uniform over the entire height of the dried film.

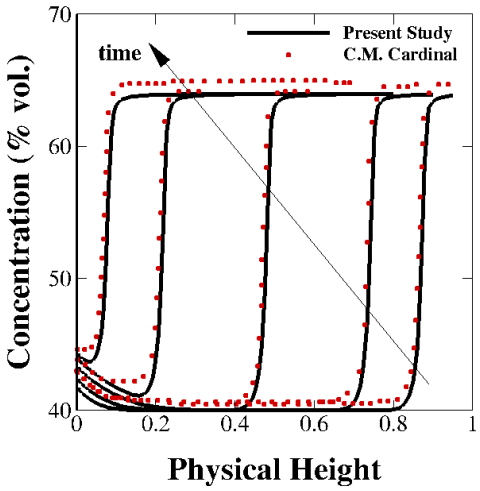

Figure 56: Validation of present model with Ns = 1, Pe = 10

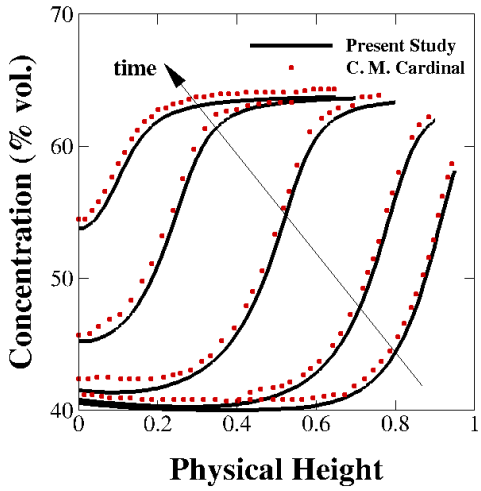

Figure 57: Validation of present model with Ns = 1, Pe = 1

In the above validation, it should be noted that the reference model does not take into account the volume fraction of the conductive additive and binder. Therefore, it does not account for the effective density and porosity.

In this study, DI water is used as the solvent for Aqueous Processing as previously mentioned in Chapter II. Since the non-dimensional equations is dependent on Peclet (Pe) and Sedimentation number (N_s), evaporation rates of water at different temperature had to be determined. Evaporation of water is well studied in and various studies have tried to develop empirical relations based on temperature, humidity, air velocity and diameter of the vessel, based on Fick's diffusion law. Evaporation of water is the diffusion of water molecules, which come out of the water surface into the air [79-85]. Since the electrodes are porous, drying of cement was used as an analogous to

gather possible empirical relationship that will allow for calculation of evaporation rates [86-88].

$$E = \left(\frac{D_w M}{RT\rho_{water}} \left(\frac{p_{w0}(1-RH)}{\delta} \right) \right) \tag{3.27}$$

$$p_{w0} = 611.21(1.0007 + 3.46E-8p_w)e^{\frac{17.502(T-273.15)}{T-32.18}} \tag{3.28}$$

$$D_w = -2.775E-6 + (4.479E-8)T + (1.656E-10)T^2 \tag{3.29}$$

where, D_w is the diffusion coefficient of water molecules leaving the film of water into the air, p_w is the atmospheric pressure and δ is the film thickness created by the water. The empirical relationship developed above, allows to calculate the flux of water molecules from the surface of a thin film, dependent on water vapor pressure and temperature is developed, that allows estimating the expected trends for the increase in evaporation rates with respect to temperature [89, 90]. The effect of Relative Humidity (RH) and temperature on the rate of evaporation can be seen in Figure 58 based on the equations above. This allows us to estimate the possible non-dimensional numbers for the model as illustrated in Table 3.

T[˚C]	Pe_{sed}	Pe	N_s
25	$2.69*10^{-1}$	$\mathbf{7.24*10^{2}}$	$3.71*10^{-4}$
50	$1.35*10^{-1}$	$\mathbf{2.67*10^{3}}$	$5.08*10^{-4}$
70	$9.42*10^{-1}$	$\mathbf{3.46*10^{3}}$	$2.73*10^{-5}$

Table 3: Non-dimensional inputs for water at different temperatures

Table 3 shows that electrode sheet drying for Aqueous Processing is going to be evaporation dominant, such that sedimentation will play no significant role. This can be witnessed graphically as seen in Figure 59, where the Sedimentation number is substantially lower than Peclet number, implying that electrode drying will always be in evaporation dominant.

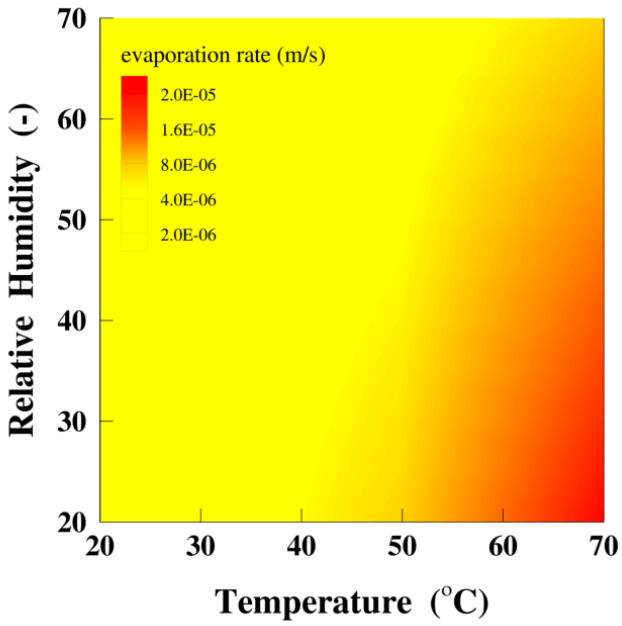

Figure 58: Evaporation rate as a function of temperature (˚C) and relative humidity (-)

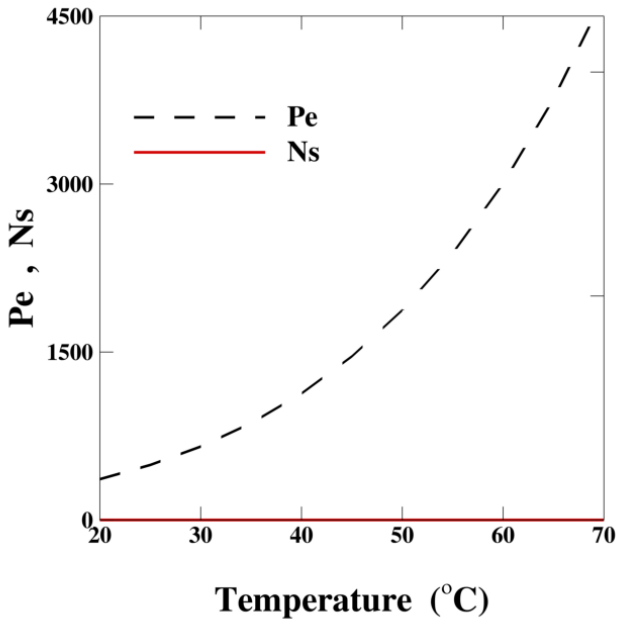

Figure 59: Comparison between Peclet and Sedimentation numbers at different drying temperature

At higher drying temperature, the constituent particles will have less time to settle down and will lead to a higher volume fraction on the top surface as seen in Figure 60 and Figure 61. Therefore, based on actual experimental initial volume fraction of active material, conductive additive and binder, the drying model corroborates the physical patterns observed in SEM for electrode sheets created using Aqueous Processing at 70˚C and 50˚C.

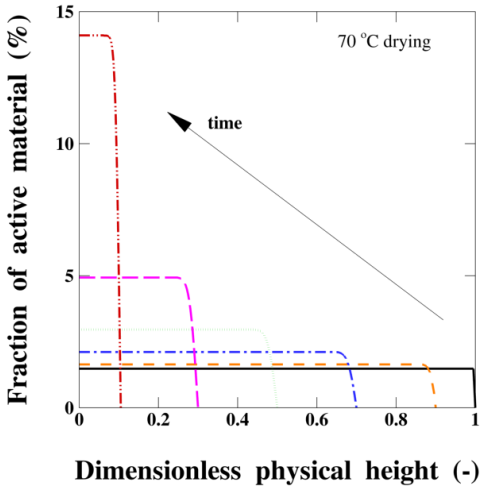

Figure 60: Volume fraction evolution with Aqueous Processing at 70˚C

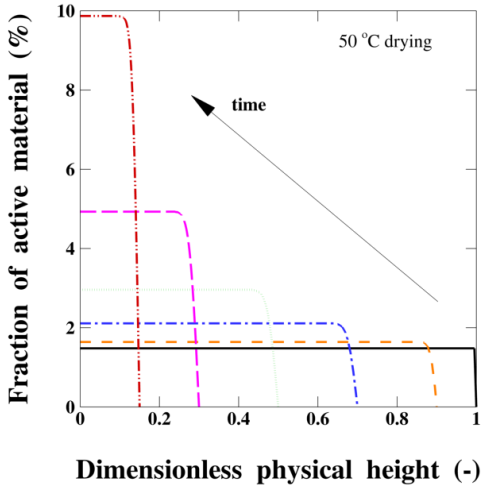

Figure 61: Volume fraction evolution with Aqueous Processing at 50˚C

At the surface of the dried film, the active materials are going to be remaining suspended, and neither sedimentation nor diffusion will disrupt the surface homogeneity observed at the top of the film. Therefore, at higher drying temperatures, the active material accumulates more towards the top surface, thereby creating a higher volume fraction. Even though the top surface of the electrode can reach the maximum possible volume fraction, it can potentially lead to the formation of a surface with a varying level of surface homogeneity. Therefore, as mentioned above, the purpose of the model is to show a qualitative analysis of evaporation is affecting the electrode structure. As seen from the SEM images, a higher drying regime does lead to more active material to be suspended on the top surface.

A similar approach was used to corroborate the model for Organic Processing dried at 50˚C. Since NMP is a volatile liquid, its evaporation rate is standardized against the rate of n-butyl acetate (0.06) and water as compared to n-butyl-acetate is 0.3 [91-93]. Using the evaporation data calculated above, it was observed that sedimentation also is very slow as compared to the evaporation of NMP as seen in electrode sheets created using Organic Processing as seen in Figure 62.

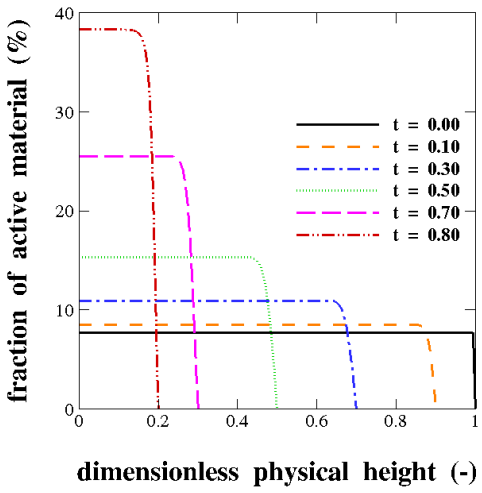

Figure 62: Volume fraction evolution with Organic Processing at 50˚C

As it has been shown above, the model indicates that evaporation rate is highly dominating. Even though the evaporation rate of NMP is much lower as compared water at the 50˚C, the slurry is still dried in an evaporation dominant regime. At the surface of

the dried film, the active materials are going to be remaining suspended, and neither sedimentation nor diffusion will disrupt the surface homogeneity observed at the top of the film. Therefore, at higher drying temperatures, the active material accumulates more towards the top surface, thereby creating a higher volume fraction. A summary of the volume fraction for Organic and Aqueous Processing under different drying temperature can be seen in Figure 63.

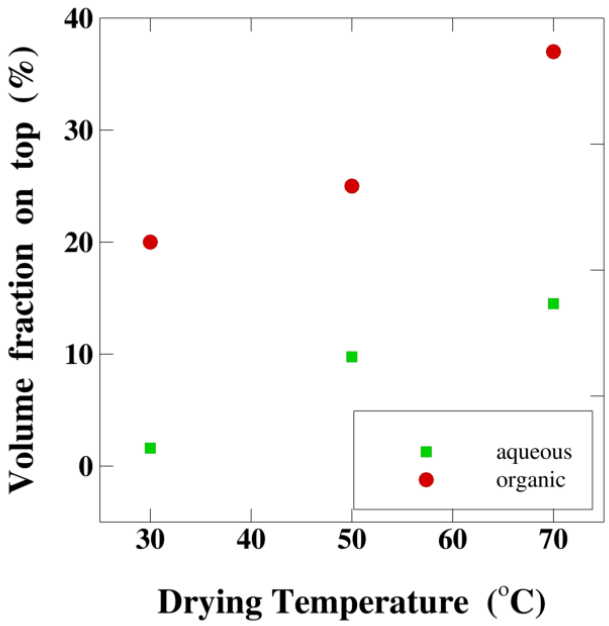

Figure 63: Volume fraction evolution at the top surface at different drying temperature with Organic and Aqueous Processing

Therefore, the above results indicate the importance of evaporation rate on the evolution of the electrode microstructure. The data indicates that when electrode slurries for LIBs dry, the final state of the electrode is highly impacted by the rate of evaporation of the solvent. It was also shown that diffusion and sedimentation have a very low effect on electrode structure in an evaporation dominant regime, thereby leading to more material to be at the surface of the electrode as seen previously.

CHAPTER IV

SUMMARY AND FUTURE RECOMMENDATIONS

A processing technique was developed in this study to use Deionized water as a solvent in the production of cathodes for Lithium-Ion Batteries. The processing technique in this study uses cheap and environmentally friendly material, requires no additional pre-treatment of aluminum foil and produces repeatable and comparable with its Organic Processing counterpart.

The processing technique presented in this work can be implemented at different drying temperatures and several combinations of compositions. The effect of drying temperature and compositions is shown to have an engineering tradeoff between creating a uniform structure, particle agglomeration and resulting performance. A qualitative analysis of SEM images shows the macroscopic observations of dried electrode sheets and consequently a comparison in their performances.

A 1-D drying model provides an evolution of the volume fraction as the casted electrode slurry dries on the aluminum foil. The single-phase model provides qualitative insights into the distribution of active material inside the electrode and corroborates the experimental results seen through the SEM images and performance.

Further studies should look into the optimization of the processing steps in regards to drying time and conditions to understand the effect of humidity and temperature in the overall formation of the electrode. The processing technique presented in this work has the potential to be applied to different active materials and

conductive additives with necessary optimizations. Hence, this study could be further extended to using different salts of lithium and different types of conductive additives showing the flexibility and versatility of the present Aqueous Processing. Analysis of adhesion using quantitative analysis is also of great importance to further corroborate the adhesion of dried slurry on the current collector. Further studies can develop a multi-phase model to investigate the evolution of the volume fraction of all components of the electrode slurry, which would shed more light on the overall microstructure developed and possible performance predictions. The 1-D model discussed in this study will be modified as part of a future study to incorporate the mobility of other particles such as carbon additive, binder and dispersant. This will provide a better understanding of distribution of these other particles and how the dominant evaporation-drying regime impacts the overall evolution of the final microstructure.

Lastly, any work of this nature requires experimental verification. Future work includes the use of X-ray microtomography to create a 3-D visualization of the electrodes. This will shed light on the electrode structure created across the height of the final dried film. SEM images only give a top view of the electrode structure therefore, for chemical mapping of the exposed electrode structure, Energy-dispersive X-ray spectroscopy has to be conducted. This will shed light on the materials that are observed in SEM images shown previously and will allow to further comment on surface homogeneity and surface craters. These tests were are still pending due to a lack of sufficient time.

REFERENCES

1. J. M. Tarascon and M. Armand, *Nature*, **414**, 359 (2001).

2. R. Wagner, N. Preschitschek, S. Passerini, J. Leker and M. Winter, *J Appl Electrochem*, **43**, 481 (2013).

3. M. Winter and R. J. Brodd, *Chemical Reviews*, **104**, 4245 (2004).

4. B. Dunn, H. Kamath and J.-M. Tarascon, *Science*, **334**, 928 (2011).

5. S. Vazquez, S. M. Lukic, E. Galvan, L. G. Franquelo and J. M. Carrasco, *IEEE Transactions on Industrial Electronics,* **57**, 3881 (2010).

6. P. B. Balbuena and Y. Wang, *Lithium-Ion Batteries: Solid Electrolyte Interphase,* Imperial College Press (2004).

7. K. Kang, Y. S. Meng, J. Bréger, C. P. Grey and G. Ceder, *Science*, **311**, 977 (2006).

8. Y.-H. Huang, K.-S. Park and J. B. Goodenough, *J Electrochem Soc*, **153**, A2282 (2006).

9. J. Bates, N. Dudney, B. Neudecker, A. Ueda and C. Evans, *Solid State Ionics*, **135**, 33 (2000).

10. Y.-H. Chen, C.-W. Wang, X. Zhang and A. M. Sastry, *J Power Sources*, **195**, 2851 (2010).

11. H. Zheng, J. Li, X. Song, G. Liu and V. S. Battaglia, *Electrochim Acta*, **71**, 258 (2012).

12. G. Liu, H. Zheng, X. Song and V. S. Battaglia, *J Electrochem Soc*, **159**, A214 (2012).

13. C. D. Rahn and C.-Y. Wang, *Battery Systems Engineering*, John Wiley & Sons (2013).

14. L. Lu, X. Han, J. Li, J. Hua and M. Ouyang, *J Power Sources*, **226**, 272 (2013).

15. M. Yoshio, R. J. Brodd and A. Kozawa, *Lithium-Ion Batteries*, Springer (2009).

16. J. L. Li, B. L. Armstrong, J. Kiggans, C. Daniel and D. L. Wood, *Langmuir*, **28**, 3783 (2012).

17. D. Wood III, *DOE Annual Merit Review (May 13-17, 2013)* (2013).

18. J. Newman and K. E. Thomas-Alyea, *Electrochemical Systems*, John Wiley & Sons (2012).

19. C. Daniel and J. O. Besenhard, *Handbook of Battery Materials*, John Wiley & Sons (2012).

20. Y. Wang and G. Cao, *Advanced Materials*, **20**, 2251 (2008).

21. M. StanleyáWhittingham, *Dalton Transactions*, 5424 (2008).

22. P. G. Bruce, B. Scrosati and J. M. Tarascon, *Angewandte Chemie International Edition*, **47**, 2930 (2008).

23. C. R. Sides and C. R. Martin, in *Modern Aspects of Electrochemistry No. 40*, p. 75, Springer (2007).

24. Y. G. Guo, J. S. Hu and L. J. Wan, *Advanced Materials*, **20**, 2878 (2008).

25. S. Franger, C. Bourbon and F. Le Cras, *J Electrochem Soc*, **151**, A1024 (2004).

26. S. Franger, F. Le Cras, C. Bourbon and H. Rouault, *Electrochemical and Solid-State Letters*, **5**, A231 (2002).

27. D. L. Wood, J. L. Li and C. Daniel, *J Power Sources*, **275**, 234 (2015).

28. J. L. Li, C. Daniel and D. Wood, *J Power Sources*, **196**, 2452 (2011).

29. B. Wang, Q. Wang, B. Xu, T. Liu, D. Wang and G. Zhao, *RSC Advances*, **3**, 20024 (2013).

30. H. H. Zheng, J. Li, X. Y. Song, G. Liu and V. S. Battaglia, *Electrochim Acta*, **71**, 258 (2012).

31. B. Akesson and B. A. G. Jonsson, *Drug Metab Dispos*, **25**, 267 (1997).

32. J. L. Li, C. Rulison, J. Kiggans, C. Daniel and D. L. Wood, *J Electrochem Soc*, **159**, A1152 (2012).

33. B. Jönsson and B. Åkesson, *International Archives of Occupational and Environmental Health*, **76**, 267 (2003).

34. S. A. Keener, R. Wrbitzky and M. Bader, *International Archives of Occupational and Environmental Health*, **80**, 327 (2007).

35. S. Langworth, H. Anundi, L. Friis, G. Johanson, M.-L. Lind, E. Söderman and B. Åkesson, *International Archives of Occupational and Environmental Health*, **74**, 213 (2001).

36. S. V. Lucas and F. C. Kopfler, *GC/MS Analysis of Organics in Drinking Water Concentrates and Advanced Waste Treatment Concentrates: Volume 3. Batch Liquid-liquid Extraction and Analysis of 10-liter Sample and Analysis of Concentrates for Small Volumes (10 to 50 Liters) of Drinking Water*, US Environmental Protection Agency, Office of Research and Development, Health Effects Research Laboratory (1984).

37. S. Lesage, *Fresenius' Journal of Analytical Chemistry*, **339**, 516 (1991).

38. C.-H. Lan, C.-Y. Peng and T.-S. Lin, *Bulletin of Environmental Contamination and Toxicology*, **73**, 392 (2004).

39. J. G. Frye, J. E. Holladay, M. A. Lilga, D. S. Muzatko, T. A. Werpy, J. F. White and A. H. Zacher, *Novel Multistep Process for Production of N-Methyl-2-Pyrrolidone from Renewable Resources*.

40. A. Bertola, Process for the production of N-methyl pyrrolidone, in, Google Patents (2001).

41. S. D. Water, *California Code of Regulations, Sections*, **25249** (1986).

42. G. M. Solomon, E. P. Morse, M. J. Garbo and D. K. Milton, *Journal of Occupational and Environmental Medicine*, **38**, 705 (1996).

43. A. M. Saillenfait, F. Gallissot and G. Morel, *Food and Chemical Toxicology*, **41**, 583 (2003).

44. B. Akesson, (2001).

45. xc, B. kesson, M. A. Carnerup, xf and B. A. G. nsson, *Scandinavian Journal of Work, Environment & Health*, **30**, 306 (2004).

46. J. L. Li, B. L. Armstrong, J. Kiggans, C. Daniel and D. L. Wood, *J Electrochem Soc*, **160**, A201 (2013).

47. J.-H. Lee, S. Lee, U. Paik and Y.-M. Choi, *J Power Sources*, **147**, 249 (2005).

48. J.-H. Lee, J.-S. Kim, Y. C. Kim, D. S. Zang and U. Paik, *Ultramicroscopy*, **108**, 1256 (2008).

49. J.-H. Lee, J.-S. Kim, Y. C. Kim, D. S. Zang, Y.-M. Choi, W. I. Park and U. Paik, *Electrochemical and Solid-State Letters*, **11**, A175 (2008).

50. E. Ligneel, B. Lestriez, A. Hudhomme and D. Guyomard, *J Electrochem Soc*, **154**, A235 (2007).

51. A. Salimi and A. A. Yousefi, *Polymer Testing*, **22**, 699 (2003).

52. A. Guerfi, M. Kaneko, M. Petitclerc, M. Mori and K. Zaghib, *J Power Sources*, **163**, 1047 (2007).

53. E. Pohjalainen, S. Räsänen, M. Jokinen, K. Yliniemi, D. A. Worsley, J. Kuusivaara, J. Juurikivi, R. Ekqvist, T. Kallio and M. Karppinen, *J Power Sources*, **226**, 134 (2013).

54. S. Lux, F. Schappacher, A. Balducci, S. Passerini and M. Winter, *J Electrochem Soc*, **157**, A320 (2010).

55. Z. Cai, Y. Liang, W. Li, L. Xing and Y. Liao, *J Power Sources*, **189**, 547 (2009).

56. J.-T. Lee, Y.-J. Chu, F.-M. Wang, C.-R. Yang and C.-C. Li, *Journal of Materials Science*, **42**, 10118 (2007).

57. W. Porcher, B. Lestriez, S. Jouanneau and D. Guyomard, *J Power Sources*, **195**, 2835 (2010).

58. M. Stein, C. Chen, D. Robles, C. Rhodes and P. Mukherjee, *Journal of Visualized Experiments: JoVE* (2016).

59. J. L. Allen, T. R. Jow and J. Wolfenstine, *Chem Mater*, **19**, 2108 (2007).

60. A. Deb, U. Bergmann, E. J. Cairns and S. P. Cramer, *The Journal of Physical Chemistry B*, **108**, 7046 (2004).

61. M. C. Tucker, M. M. Doeff, T. J. Richardson, R. Finones, E. J. Cairns and J. A. Reimer, *Journal of the American Chemical Society*, **124**, 3832 (2002).

62. S. Zhu, H. Zhou, T. Miyoshi, M. Hibino, I. Honma and M. Ichihara, *Advanced Materials*, **16**, 2012 (2004).

63. M. M. Doeff, J. D. Wilcox, R. Kostecki and G. Lau, *J Power Sources*, **163**, 180 (2006).

64. H. Gabrisch, J. Wilcox and M. M. Doeff, *Ecs Transactions*, **3**, 29 (2007).

65. D. Wang, H. Li, S. Shi, X. Huang and L. Chen, *Electrochim Acta*, **50**, 2955 (2005).

66. J. Valli, *Journal of Vacuum Science & Technology A*, **4**, 3007 (1986).

67. B. Son, M. H. Ryou, J. Choi, T. Lee, H. K. Yu, J. H. Kim and Y. M. Lee, *Acs Appl Mater Inter*, **6**, 526 (2014).

68. S. Nakanishi, T. Suzuki, Q. Cui, J. Akikusa and K. Nakamura, *Transactions of Nonferrous Metals Society of China*, **24**, 2314 (2014).

69. K. Li, X. Geng, J. Simonsen and J. Karchesy, *Int J Adhes Adhes*, **24**, 327 (2004).

70. P. Benjamin and C. Weaver, *Proceedings of the Royal Society of London A: Mathematical, Physical and Engineering Sciences*, **254**, 163 (1960).

71. W. Porcher, B. Lestriez, S. Jouanneau and D. Guyomard, *J Power Sources*, **195**, 2835 (2010).

72. C. M. Cardinal, Y. D. Jung, K. H. Ahn and L. F. Francis, *Aiche J*, **56**, 2769 (2010).

73. A. F. Routh and W. B. Zimmerman, *Chem Eng Sci*, **59**, 2961 (2004).

74. R. E. Trueman, E. L. Domingues, S. N. Emmett, M. W. Murray and A. F. Routh, *J Colloid Interf Sci*, **377**, 207 (2012).

75. C. Song, P. Wang and H. A. Makse, *Nature*, **453**, 629 (2008).

76. A. Donev, I. Cisse, D. Sachs, E. A. Variano, F. H. Stillinger, R. Connelly, S. Torquato and P. M. Chaikin, *Science*, **303**, 990 (2004).

77. M. Kaviany, *Principles of Heat Transfer in Porous Media*, Springer Science & Business Media (2012).

78. H. Rumpf and A. Gupte, *NASA STI/Recon Technical Report N*, **75**, 30484 (1975).

79. K. Hisatake, S. Tanaka and Y. Aizawa, *Journal of Applied Physics*, **73**, 7395 (1993).

80. K. Hisatake, M. Fukuda, J. Kimura, M. Maeda and Y. Fukuda, *Journal of Applied Physics*, **77**, 6664 (1995).

81. P. Coussot, *The European Physical Journal B-condensed Matter and Complex Systems*, **15**, 557 (2000).

82. M. Bakhshi, B. Mobasher and C. Soranakom, *Construction and Building Materials*, **30**, 413 (2012).

83. N. A. Fuchs, *Evaporation and Droplet Growth in Gaseous Media*, Elsevier (2013).

84. E. H. Kennard, (1938).

85. H. Garbalińska, *Cement and Concrete Research*, **36**, 1294 (2006).

86. J. M. Torrenti, L. Granger, M. Diruy and P. Genin, *Materials Journal*, **96**, 35 (1999).

87. R. P. West and N. Holmes, *Construction and Building materials*, **19**, 674 (2005).

88. J.-K. Kim and C.-S. Lee, *Cement and Concrete Research*, **28**, 985 (1998).

89. P. R. Wiederhold, *Water Vapor Measurement: Methods and Instrumentation*, CRC Press (1997).

90. R. E. Bolz and G. L. Tuve, *CRC Handbook of Tables for Applied Engineering Science (edn)*, in, CRC Press, Boca Raton, FL (1973).

91. D. Kimpton and F. Wall, *The Journal of Physical Chemistry*, **56**, 715 (1952).

92. G. Lugg, *Analytical Chemistry*, **40**, 1072 (1968).

93. K. Kwon, T. Ibrahim, Y. Park and C. Simmons, *Advances in Environmental Research*, **8**, 667 (2004).